Development and evaluation of CO_2 transport in MPAS-A v6.3

Tao Zheng[1], Sha Feng[2], Kenneth J. Davis[2], Sandip Pal[3], and Josep Anton Morguí[4]

[1]Department of Geography & Institute of Great Lake Research, Central Michigan University, Mount Pleasant, MI. USA
[2]Department of Meteorology and Atmospheric Science, The Pennsylvania State University, University Park, PA. USA
[3]Department of Geosciences, Texas Tech University, Lubbock, TX. USA
[4]Environmental Science and Technology Institute, Universitat Autònoma de Barcelona, ICTA-UAB, Bellaterra, Spain

Correspondence to: Tao Zheng (zheng1t@cmich.edu)

Abstract.

Chemistry transport models (CTM) play an important role in understanding fluxes and atmospheric distribution of carbon dioxide (CO_2). They have been widely used for modeling CO_2 transport through forward simulations and inferring fluxes through inversion systems. With the increasing availability of high resolution observations, it has been become possible to estimate CO_2 fluxes at higher spatial resolution. However the computational cost of high resolution global model simulation is so high that only major research and operation centers can afford it. In this paper, we implemented CO_2 transport in Model Prediction Across Scales-Atmosphere (MPAS-A). The objective is to use the variable-resolution capability of MPAS-A to enable high resolution CO_2 simulation at limited region with a global model. Treating CO_2 as an inert tracer, we implemented in MPAS-A (v6.3) the CO_2 transport processes, including advection, vertical mixing by boundary layer scheme, and convective transport. We evaluated the newly implemented model by running two sets of simulations over a 60-15 km variable-resolution global domain. The first set of simulations covers four Atmospheric Carbon and Transport-America (ACT-America) aircraft campaign seasons (2016-2018), and the simulated CO_2 is evaluated using the extensive airborne measurements from ACT. The simulation accuracy is also compared with a 27-km resolution WRF-Chem simulation and CarbonTracker (v2019) covering the same time periods. The second set of simulations covers the month of January and July of 2014, and the results are evaluated using near-surface hourly CO_2 measurements from 50 surface and tower sites across the globe. This simulation accuracy is compared with European Center for Medium-Range Weather Forecasts (ECMWF) Integrated Forecasting System (IFS) global simulation conducted during the same period. Overall, the evaluation using aircraft measurements indicates that MPAS CO_2 transport model is capable of representing the observed atmospheric CO_2 structures related with the mid-latitude synoptic weather system, including the warm/cold sector distinction, boundary layer to free troposphere difference, and CO_2 enhancements along frontal boundaries. The evaluation using hourly measurements shows that the MPAS CO_2 transport model is capable of achieving a same level of accuracy as the IFS 80-km resolution simulation.

1 Introduction

Carbon dioxide (CO_2) is the most important greenhouse gas, and our knowledge about its sources and sinks still have large gaps. Inversion systems are often used to infer CO_2 fluxes based on observations and chemistry transport models (CTM). Two

types of CTMs are commonly used: global models and regional models. Global models are commonly used for inferring CO_2 fluxes at coarse spatial scale (Patra et al., 2008; Schuh et al., 2019; Jacobson et al., 2007, 2020). With the fast increasing number of atmospheric CO_2 observations, including those acquired by ground based, airborne, and satellite instruments, regional inversion system have been developed and applied to estimate carbon fluxes at higher resolution (Gerbig et al., 2009; Pillai et al., 2012; Lauvaux et al., 2012; Hu et al., 2019; Zheng et al., 2018, 2019).

A major challenge of atmospheric CO_2 inversion modeling is how to partition the model-data mismatch (MDM) among the transport model error, observation error, and prior flux error. In the Bayesian inversion framework, the error covariance matrix $\mathbf{R}$ is commonly used to represent the combined error of transport model and observations. While it is important to correctly represent the transport model error in an inversion system, it is also important to reduce the error in order to estimate the fluxes with less uncertainty. One approach to reduce transport model error is to increase simulation resolution. For instance, Feng et al. (2016) found high-resolution WRF-Chem simulation improved CO_2 model-data comparison because of better resolved planetary boundary layer and better representation of spatial variability of CO_2 fluxes. In a recent study, Agusti-Panareda et al. (2019) investigated the impacts of transport model's horizontal resolutions on simulated CO_2 accuracy, and they found that CO_2 variability are generally better represented by higher resolution simulations.

Global high resolution CO_2 simulations require large computational resources which may not be affordable outside major research and operational centers. Regional (limited area) models, which circumvent the high computational cost of global models, are often used for high resolution CO_2 transport (Feng et al., 2016; Diaz-Isaac et al., 2019, 2018) and inverse modeling (Sarrat et al., 2007; Gerbig et al., 2008; Lauvaux et al., 2012; Zheng et al., 2019). However a regional model requires CO_2 transported from outside its model domain to be prescribed. For a CO_2 inversion system, having lateral boundaries increase the size of the control vector to be optimized (Rayner et al., 2019). A number of approaches have been applied to the CO_2 lateral boundary problem, such as assuming the boundary inflow is perfectly known (Gockede et al., 2010), correcting the lateral boundary condition using observation prior to inversion (Lauvaux et al., 2012; Schuh et al., 2013), or jointly optimizing flux and lateral boundary condition (Zheng et al., 2018). When CO_2 lateral boundary is optimized, an inversion system adjusts its CO_2 fields at the boundary prescribed by a parent global model in addition to adjusting surface fluxes. This could be problematic for inversion systems that use satellite derived column averaged CO_2 measurements (XCO_2) because model-data mismatches in the free troposphere are often originated from outside a regional model's limited area domain (Feng et al., 2019; Lauvaux and Davis, 2014).

The objective of the present paper is to provide an alternative high-resolution CO_2 transport modeling approach to regional transport models. This approach is to use a global variable-resolution model which allows for local grid refinement that enables high resolution simulation over interested region without incurring the prohibitively high computational cost or the lateral boundary condition. Variable-resolution through local grid refinement has been widely used in Numerical Weather Prediction (NWP) models, such as MPAS (Skamarock et al., 2012), Ocean-Land-Atmosphere Model (OLAM) (Walko and Avissar, 2008a,

b), Energy Exascale Earth System Model (E3SM) (Golaz et al., 2019), and Finite-Volume Cubed-Sphere model(FV3) (Putman and Lin, 2007). One benefit of local mesh refinement is enabling regional high-resolution modeling without incurring the lateral boundary condition and its associated problems, such as solution mismatches between the driving global model and the evolving regional model (Davies, 2014).

Model Prediction Across Scales-Atmosphere (MPAS-A) is a fully compressible non-hydrostatic global atmospheric model which uses finite-volume numeric solver discretized on centroidal Voronoi mesh with C-grid staggering of its prognostic variables (Skamarock et al., 2012; Thuburn, 2007; Ringler et al., 2010). The centroidal Voronoi mesh allows for local refinement and variable-resolution horizontal mesh which can be gradually changed from coarse to fine resolutions (Skamarock et al.,
10 2012; Ringler et al., 2008).

To enable CO_2 transport modeling, we implemented in MPAS-A (v6.3) the CO_2 transport processes, including advection, vertical mixing by Planetary Boundary Layer (PBL) scheme, and convective transport. We used the newly developed model to conduct two sets of simulations over a 60-15 km variable-resolution global domain. Then the simulation results are evaluated
15 using an extensive set of airborne observations over the eastern United States and near-surface observations from surface and tower stations across the globe. The simulation accuracy of MPAS is compared with three established CO_2 modeling systems based on the same observational data: WRF-Chem (Skamarock et al., 2008; Feng et al., 2019), Carbontracker (v2019, CT2019 hereafter) (Jacobson et al., 2020) , and ECWMF IFS (Agusti-Panareda et al., 2014, 2019).

20   The remainder of the paper is organized as follows. Section 2 details the implementation of CO_2 transport in MPAS, Section 3 describes MPAS CO_2 simulation experiments and evaluation using airborne and near-surface observations, and comparison with WRF-Chem, CT2019, and IFS. Section 4 provides a summary of the model development and evaluations.

2 Implementation of CO_2 transport in MPAS

This section describes the major modifications to MPAS that we made to implement CO_2 tracer transport. We represent CO_2
25 by its dry air mixing ratio (q_{co_2}) and model its atmospheric transport by adding its continuity equation in MPAS following Eq. 7 of Skamarock et al. (2012).

$$\frac{\partial(\tilde{\rho} q_{co_2})}{\partial t} = -(\nabla \cdot \tilde{\rho} q_{co_2} \mathbf{V})_\zeta + F_{bl} + F_{cu} \qquad (1)$$

where $\tilde{\rho} = \rho_d/(\partial \zeta/\partial z)$, ρ_d is dry air density, ζ is the vertical coordinate, z is geometric height, t is time, and $\mathbf{V}$ is the velocity vector. The left hand side of the equation is the total CO_2 time tendency ($\partial(\tilde{\rho} q_{co_2})/\partial t$), and the three terms on the right
30 hand side represent the contributions from advection, vertical mixing, and convective transport respectively. CO_2 tendency

from advection is modeled in flux form (Section 2.1), while tendency from vertical mixing (F_{bl}) and convective transport (F_{cu}) are modeled in uncoupled form ($\partial q_{co_2}/\partial t$) which are coupled to $\tilde{\rho}$ before being added to the total tendency. Details of the three terms on the right hand side of Eq. 1 are described in the following sections. We note that because the monotonicity constraint in third-order scalar horizontal advection scheme (Skamarock and Gassmann, 2011) introduces dissipation MPAS does not use

5 any explicit horizontal diffusion for scalar, and we did not include horizontal diffusion for CO_2 accordingly.

2.1 CO₂ advection

Advection is the most significant component of CO_2 atmospheric transport. Following the example of other scalars in MPAS (Skamarock and Gassmann, 2011), we model CO_2 advection as:

10 $$(\nabla \cdot \tilde{\rho} q_{co_2} \mathbf{V})_\zeta = \Big[\frac{\partial(\tilde{\rho} u q_{co_2})}{\partial x} + \frac{\partial(\tilde{\rho} v q_{co_2})}{\partial y}\Big]_\zeta + \frac{\partial(\tilde{\rho} w q_{co_2})}{\partial \zeta} \tag{2}$$

where $\mathbf{V} = (u, v, w)$, and u, v, and w is the zonal, meridional, and vertical wind respectively. The first item on the right hand side enclosed in the square bracket is the CO_2 horizontal flux divergence, and second item is the vertical flux divergence. The horizontal flux divergence is transformed via the divergence theorem into an integral of flux over each control volume, which is modeled as:

15 $$\Big[\frac{\partial(\tilde{\rho} u q_{co_2})}{\partial x} + \frac{\partial(\tilde{\rho} v q_{co_2})}{\partial y}\Big]_\zeta = \frac{1}{A_i} \sum_{e}^{n_e} l_e \, F_e(\mathbf{V}_H, \tilde{\rho} q_{co_2}) \tag{3}$$

where e indexes the edges of a cell and n_e represents the number of edges the cell has, l_e is the length of an edge, A_i is the cell's areal size, $F_e(\mathbf{v}_H, \tilde{\rho} q_{co_2})$ is the instantaneous horizontal CO_2 flux that crosses the cell edge e, and $\mathbf{V}_H = (u, v)$ is the horizontal wind vector. The details of MPAS instantaneous horizontal flux calculation can found in Skamarock and Gassmann (2011). The vertical CO_2 flux divergence in Eq. 2 is calculated using finite difference

20 $$\frac{\partial(\tilde{\rho} w q_{co_2})}{\partial \zeta} = \frac{1}{\Delta \zeta}\Big[F(w, \tilde{\rho} q_{co_2})_{k+\frac{1}{2}} - F(w, \tilde{\rho} q_{co_2})_{k-\frac{1}{2}}\Big] \tag{4}$$

where $F(w, \tilde{\rho} q_{co_2})$ is the vertical CO_2 flux that crosses a cell's vertical face, and k indexes the vertical coordinate.

2.2 CO₂ vertical mixing

Like in WRF (Skamarock et al., 2008), a planetary boundary layer (PBL) parameterization in MPAS treats the vertical mixing of momentum and scalars not only in the boundary layer but in the entire atmospheric column. Yonsei University (YSU) PBL

25 scheme (Hong et al., 2006) is one of the PBL schemes available in MPAS 6.3. The present YSU scheme treats vertical mixing of momentum, potential temperature, and water species, but not atmospheric tracers. We modified the scheme to treat CO_2

vertical mixing.

In the YSU scheme, after the boudary layer (BL) top is determined, the vertical mixing of momentum, potential temperature, and water vapor are treated separately: above BL, local K-profile approach (Louis, 1979)) is used for vertical diffusion of
5   momentum and scalars (Noh et al., 2003; Hong et al., 2006). Within BL, an entrainment flux at the inversion layer is included for momentum and scalars diffusion. In addition, a countergradient mixing term is included for the diffusion of momentum and potential temperature to account for the convective-driven mixing (γ_c of Eq. 4 in Hong et al. (2006)), but this term is not used for water vapor.

10   Following the treatment of water vapor, we parameterize CO_2 vertical mixing in BL as

$$\frac{\partial q_{co_2}}{\partial t} = \frac{\partial}{\partial z}\left[K_h(\frac{\partial q_{co_2}}{\partial z}) - \overline{(w'q'_{co_2})_h}(\frac{z}{h})^3\right] \tag{5}$$

where z is the vertical distance to surface, h is BL top height, K_h is vertical eddy diffusivity. Note that this formulation does not include a countergradient mixing term following the treatment of water vapor in the original YSU (Hong et al., 2006). The second term in the square bracket of Eq. 5 represents the contribution from CO_2 entrainment flux at the inversion layer, which
15   is parameterized as:

$$\overline{(w'q'_{co_2})_h} = w_e \Delta q_{co_2}|_h \tag{6}$$

where $\Delta q_{co_2}|_h$ is the CO_2 mixing ratio difference across the inversion layer, and w_e is the entrainment rate at the inversion layer calculated by Eq. A11 of Hong et al. (2006). Above BL top, vertical mixing of CO_2 is parameterized as:

$$\frac{\partial q_{co_2}}{\partial t} = \frac{\partial}{\partial z}\left[K_h(\frac{\partial q_{co_2}}{\partial z})\right] \tag{7}$$

20   We use the same value for CO_2 eddy diffusivity as water vapor. The details of K_h calculation can be found in the appendix of Hong et al. (2006). The term $\partial q_{co_2}/\partial t$ from Eqs. 5 is coupled with dry air density before being applied to the continuity equation (Eq. 1).

2.3 CO_2 convective transport

For convective transport, we modified the Kain-Fritsch scheme (hereafter KF) (Kain, 2004) to include the CO_2 treatment.
25   KF is a mass-flux convection scheme which rearranges mass in an air column using convective updrafts, downdrafts, and environmental mass fluxes. Both the updraft and downdraft entrain from and detrain to the environment, thus altering the vertical profile of an air column's thermodynamic properties. We added the CO_2 convective transport as:

$$\frac{\partial q_{co_2}}{\partial t} = \frac{(M_u + M_d)}{\rho A}\frac{\partial q_{co_2}}{\partial z} + \frac{M_{ud}}{M}(q_{co_2}^u - q_{co_2}) + \frac{M_{dd}}{M}(q_{co_2}^d - q_{co_2}) \tag{8}$$

where q_{co_2}, $q_{co_2}^u$, and $q_{co_2}^d$ are the CO$_2$ mixing ratio in the environment, updraft, and downdraft respectively, M_u and M_d are the updraft and downdraft mass respectively, ρ is the environment air density, A is the horizontal area of a cell, $M = \rho A \delta z$ is the mass of environmental air in a grid box, and M_{ud} and M_{dd} are the detrainment from the updraft and downdraft respectively.

5   In KF, the updraft and downdraft mass and the rates for the entrainment and detrainment are determined by a steady-state plume model and a convective available potential energy (CAPE) closure assumption: 90% of the existing CAPE should be removed by the convection parameterization (Kain and Fritsch, 1990; Fritsch and Chappell, 1980; Kain, 2004). The updraft source layers are determined by a search from the model's lowest vertical level for a group of consecutive layers that is buoyant and at least 50 hPa deep (Kain, 2004). The initial value of CO$_2$ mixing ratio in the updraft is modeled as a pressure weighted
10 average of the source layers:

$$q_{co_2}^u = \sum_k \frac{\delta q_{co_2,k}\,\delta p_k}{\delta p_k} \qquad (9)$$

where δp_k is layer's pressure depth, and $q_{co_2,k}$ is the layer's CO$_2$ mixing ratio. Carbon dioxide mixing ratio of the updraft is modified by the entrainment of the environmental air through its ascent from its starting level to the cloud top.

$$q_{co_2}^u = \frac{q_{co_2}^u M_u + q_{co_2} M_{ue}}{M_u + M_{ue}} \qquad (10)$$

15 where M_{ue} is the updraft entrainment. The initial CO$_2$ mixing ratio of a downdraft ($q_{co_2}^d$) is the same as that of the environment (q_{co_2}) at the downdraft starting level and it is modified by entrainment through the downdraft descent:

$$q_{co_2}^d = \frac{q_{co_2}^d M_d + q_{co_2} M_{de}}{M_d + M_{de}} \qquad (11)$$

where M_{de} is the downdraft entrainment.

3   Model evaluation

20 In this section we evaluate the newly developed MPAS CO$_2$ transport model through simulation experiments using airborne and near-surface observations. After describing the simulation configuration (Sect. 3.1), we assess the model's global CO$_2$ mass conservation property (Sect. 3.2), then we evaluate the model accuracy by comparing MPAS simulated CO$_2$ with high-resolution airborne measurements (Sect. 3.3) and near-surface hourly measurements (Sect. 3.4). Two sets of MPAS simulations are conducted: the first set simulations covers four ACT campaign seasons (2016-2018) for evaluation using high-resolution
25 airborne measurements; the second set covers January and July of 2014 for evaluation using near-surface CO$_2$ measurements and comparison with the IFS simulation results reported in Agusti-Panareda et al. (2019). In the following model evaluation,

we use root mean square error (RMSE), bias (μ), and random error (STDE) as the model accuracy metrics:

$$\text{RMSE} = \sqrt{\frac{1}{N}\sum_{i=1}^{N}(m_i - o_i)^2} \tag{12}$$

$$\mu = \frac{1}{N}\sum_{i=1}^{N}(m_i - o_i) \tag{13}$$

$$\text{STDE} = \sqrt{\frac{1}{N}\sum_{i=1}^{N}(m_i - o_i - \mu)^2} \tag{14}$$

where o_i and m_i represent the observed and modeled values respectively.

3.1 Simulation experiment configuration

For all subsequent simulations, MPAS uses a 60-15km variable-resolution global mesh. Fig. 1 shows the cell size (in km^2) of

10 the simulation domain, where the highest resolution (15 km) over North America has cell size smaller than 250 km^2 which gradually increases to about 3,600 km^2 for the rest of the global domain. On the vertical direction, there are 55 levels spanning from surface to 30 km above the mean sea level. Model time step is 90 seconds in accordance with the highest (15km) horizontal resolution. For physical parameterizations, in addition to the modified YSU PBL (Hong et al., 2004) and Kain-Fristch cumulus schemes (Kain, 2004) described in Sect. 2, we use RRTMG for longwave and shortwave radiation (**?**), Noah

15 land scheme (Chen and Dudhia, 2001), Monin-Obukhov surface layer scheme, and WRF single-moment 6-class microphysics scheme (Hong and Lim, 2006). The third-order advection is used for all scalars and CO_2 tracer. A summary of the physics parameterizations used in the simulations is given in Table 1.

Meteorology initial conditions are generated from the ERA-Interim analysis (Dee et al., 2011). To keep model meteoro-

20 logical fields close to the analysis, MPAS meteorological fields are re-initialized using the analysis at 00:00 UTC each day throughout a simulation period. Carbon dioxide mixing ratio is kept unchanged during the meteorology re-initializations, thus a free-running simulation. This configuration is the same as that used by Agusti-Panareda et al. (2014, 2019) in their IFS global CO_2 simulations. The first CO_2 initial condition for a simulation is from CT2019 $3° \times 2°$ posterior dry mole fraction product and CO_2 fluxes are prepared by interpolating the CT2019 3-hourly $1° \times 1°$ posterior flux product (Jacobson et al., 2020). The

25 four fluxes from CT2019 (biosphere, ocean, fossil fuel, and fire) are interpolated to MPAS model grid and ingested at 3-hour intervals throughout a simulation.

3.2 CO$_2$ mass conservation

For a transport model, it is very important to maintain the global CO$_2$ mass conservation (Agusti-Panareda et al., 2017; Polavarapu et al., 2016). To evaluate the mass conservation property of MPAS, we run a 120-hour continuous simulation and examine the change of total mass of CO$_2$ in the model domain. The simulation starts at 2016-08-01 00:00 UTC and ends at

5   2016-08-06 00:00 UTC. It uses the physics parameterizations and domain setup described in Sect. 3.1. The CO$_2$ dry air mixing ratio field in the model is initialized using CT2019 dry mole fraction, but fluxes ingestion is turned off. Because the meteorology re-initiation will introduce dry air mass change which in turn will impact the total CO$_2$ mass, we run the simulation without applying the meteorology re-initialization. The impact of meteorological re-initialization and its treatment are considered in Section 3.2.2.

10 ### 3.2.1 Mass conservation without meteorology re-initialization

Through the 120-hour simulation, model outputs are saved at 1-hour intervals using double-precision. The total mass of dry air (m_{air}) and CO$_2$ (m_{co_2}) is then calculated from these hourly outputs using Eqs. 15 and 16 respectively.

$$m_{air} = \sum_{k}^{L}(\sum_{i}^{N} A_i\, h_{i,k}\, \rho_{i,k}) \tag{15}$$

15 $$m_{co_2} = \sum_{k}^{L}(\sum_{i}^{N} A_i\, h_{i,k}\, \rho_{i,k}\, q_{i,k}) \tag{16}$$

In Eqs. 15 and 16, subscript i indexes the horizontal cell, ranging from 1 to N=535,554; subscript j indexes the vertical level, ranging from 1 to L=55. MPAS hexagon cell base areal size is A_i (cell size is constant within a given column at different vertical levels), and the height of the cell is represented by $h_{i,j}$ (heights at different columns of a same vertical level maybe different due to the terrain-following vertical coordinate). The volume of a grid box is $V_{i,k} = A_i\, h_{i,k}$, its dry air density (kg/m^3)

20 is $\rho_{i,j}$, and its CO$_2$ dry air mixing ratio (kg/kg) is $q_{i,j}$.

The calculation shows that the total volume of the MPAS model domain is $1.5184682921961 \times 10^{19}$ m^3, which is a constant through the simulation because of the model's height based vertical coordinate. At the start of the simulation, the total dry air mass is $5.053906341880670208 \times 10^{18}$ kg and total CO$_2$ mass is $3.079178060337270 \times 10^{15}$ kg. The total mass of dry air

25 and CO$_2$ at each subsequent hour is normalized by their respective starting values and resulting variations are shown in Fig. 2. The maximal variation of the total dry air mass from its starting value during the 120-hour simulation is $29,660,160$ kg, which when divided by the total air volume represents a variation of mean dry air density approximately 1.95310^{-12} kg/m^3. The maximal variation of total CO$_2$ mass from its starting value is $18,980$ kg, which represents a variation in mean CO$_2$ mixing

ratio of 1.0416×10^{-15} kg/kg (equivalent to 6.839×10^{-10} ppm) for a mean dry air density of 1.2 kg/m^3.

In MPAS dry air density and CO_2 dry air mixing ratio are prognostic variables and their precision is limited by the round-off error of the model's Fortran double-precision code. Fig.2 shows that the maximal variation in dry air density is 1.95310^{-12}

5   kg/m^3) and maximal variation in CO_2 dry air mixing ratio is 1.0416×10^{-15} kg/kg during the simulation period. Given that the double precision float number calculation of MPAS Fortran code is capable of having 14 decimal places of precision, we consider the MPAS CO_2 transport maintains the global mass conservation to the level allowed by the machine precision.

3.2.2 CO_2 mass conservation during meteorology re-initialization

The last section has demonstrated that MPAS is capable of maintaining global CO_2 mass conservation. However when me-
10   teorology re-initialization is applied, dry air density fields in the model are replaced by values from the initialization files generated from the ERA-Interim analysis (Dee et al., 2011). In most cases, this will cause dry air density change which in turn will introduce CO_2 mass change because CO_2 dry air mixing ratios are kept unchanged during the re-initializations.

To assess this possible change in global CO_2 mass, we conducted a 48-day MPAS simulation starting 00:00 UTC 15 July
15   2016 with meteorology re-initialization at 24-hour interval but without CO_2 fluxes ingestion. The global CO_2 mass is calcu-
lated using Eq. 16 at the end of each 24-hour period which is then compared with its initial value at the start of the simulation.
The resulting global CO_2 mass variation is shown in the top panel of Fig. 3. The figure shows that during the 48-day simula-
tion, the maximal variation of total CO_2 mass can reach approximately $\pm 0.05\%$, which is 7 to 8 magnitudes larger than that
without re-initialization (Fig. 2). To restore the CO_2 mass conservation, we calculate the total CO_2 mass difference caused by
20   a meteorology re-initialization using

$$r = \frac{\sum_k^L (\sum_i^N A_i \, h_{i,k} \, \rho_{i,k} \, q_{i,k})}{\sum_k^L (\sum_i^N A_i \, h_{i,k} \, \rho'_{i,k} \, q_{i,k})} \qquad (17)$$

where notations are the same as in Eq. 16 except that $\rho'_{i,k}$ is the dry air density after a meteorology re-initialization and $\rho_{i,k}$ is the value before the re-initialization. Then CO_2 mixing ratio at each grid box is scaled by

$$q'_{i,k} = r \times q_{i,k} \qquad (18)$$

25   where $q'_{i,k}$ is the CO_2 mixing ratio that will be used as the initial value for the next 24-hour simulation period.

To test the effectiveness of this scaling method, the 48-day simulation is conducted again but with the CO_2 mixing ratio scaling after each re-initialization using Eqs. 17 and 18. The resulting variation in total CO_2 mass is plotted at the lower panel of Fig. 3. The figure shows that maximal variation is less than $\pm 0.001\%$, which is small enough to be acceptable for most CO_2

transport simulations. We note that an alternative approach is to scale CO_2 mixing ratio at each grid box individually by

$$q'_{i,k} = \frac{\rho_{i,k}}{\rho'_{i,k}} \times q_{i,k} \tag{19}$$

where notation is the same as Eq. 17. This scaling approach can maintain total CO_2 mass conservation as allowed by machine precision but it will introduce artificial spatial variations in CO_2 mixing ratio. In the simulations in the following sections, we

5 chose to use the first scaling approach to avoid the artificial CO_2 mixing ratio variation by accepting the small change in total CO_2 mass.

3.3 Model valuation using airborne measurements

In this section, we evaluate the MPAS CO_2 simulation accuracy using an extensive high resolution CO_2 observation data acquired through the Atmospheric Carbon and Transport-America project (ACT-America, henceforth, referred to as ACT). ACT

10 is a National Aeronautics and Space Administration (NASA) Earth Venture Suborbital 2 (EVS-2) mission, and its goal is to improve atmospheric inversion estimates of CO_2 and CH_4 through extensive airborne measurements over the eastern United Stated during multiple seasons (Davis et al., 2018a). Through four campaign seasons from Summer 2016 to Spring 2018 with two research aircraft (C130 and B200), the ACT project has collected an extensive dataset of highly resolved CO_2 measurements in both boundary layer and free troposphere. To use ACT airborne CO_2 measurements for model evaluation, we ran

15 four sets of MPAS simulations each covering one ACT campaign season. The duration of the ACT campaign seasons and the corresponding MPAS simulation periods is given in Table 2. All simulations use the same domain and configurations as described in Sect. 3.1, and model outputs are saved at 1-hourly interval for subsequent evaluation.

3.3.1 Evaluation of modeled horizontal wind fields

20 Accurate meteorological fields are critical for an accurate CO_2 transport simulation. Michaelis et al. (2019) has assessed MPAS simulated meteorology accuracy using extensive observation data. Before evaluating the simulated CO_2, we first evaluate the MPAS simulated horizontal wind fields considering their importance in CO_2 advection. We compare MPAS simulated horizontal wind fields at 00:00 and 12:00 UTC each day of the simulation period with raidosonde observations from 457 stations located around the globe at four pressure levels (1,000, 850, 500, 850, and 200 hPa). The locations of the 457 radiosonde

25 stations are shown in Fig. S3 of the supplement material. The horizontal wind fields evaluation results for each of the four ACT seasons are summarized in Table 6. For instance, the RMSE of vector wind at the 1000, 850, 500, and 200 hPa are 3.31, 3.87,3.78, and 5.46 m/s for the Summer 2016 season. These values are comparable to but higher than the vector wind RMSE of the month of July 2014 from the IFS 9km and 80km horizontal resolution global simulations reported in Agusti-Panareda et al. (2019). For the winter 2017 season, RMSE of vector wind is 3.70, 4.44, 4.56, and 5.40 m/s respectively at the four pressure

30 levels, and they are slightly higher than the January 2014 vector wind RMSE reported in Agusti-Panareda et al. (2019). The

error statistics from the other two seasons are of similar magnitude as the summer 2016 and winter 2017 seasons.

3.3.2 Overall accuracy of MPAS modeled CO_2

We use the ACT airborne measurements to evaluate MPAS CO_2 simulation regarding its overall accuracy and its performance
measured by three model evaluation metrics proposed by Pal et al. (2020). To provide an objective reference, we also compare
MPAS performance with two established CO_2 model systems: WRF-Chem (Skamarock et al., 2008) and CT2019 (Jacobson
et al., 2020) using the same set of airborne measurements.

WRF-Chem is an online chemistry transport model based on the regional NWP WRF (Grell et al., 2011; Skamarock et al.,
2008). WRF-Chem simulations have been carried out at 27 km horizontal grid over North America as a part of the ACT
project (Feng et al., 2020). The WRF-Chem simulations use ERA5 reanalysis (Hersbach et al.) for meteorological initial and
boundary conditions, CarbonTracker (Jacobson et al., 2007) posterior mole fraction for CO_2 initial and boundary conditions,
and CarbonTracker posterior fluxes for CO_2 fluxes. The WRF-Chem simulations use meteorological nudging and 120-hour
meteorological re-initialization to keep meteorological fields close to the analysis. CarbonTracker (Jacobson et al., 2007, 2020)
is an operational carbon data-assimilation system which uses Transport Model 5 (TM5) (Krol et al., 2005) for atmosphere
transport. TM5 is an offline global chemical transport model which includes CO_2 advection, deep and shallow convection, and
vertical diffusion in both the planetary boundary layer and free troposphere (Krol et al., 2005). In producing CT2019 CO_2
mole fraction (Jacobson et al., 2020), TM5 simulation ran over a $3° \times 2°$ global domain and an nested $1° \times 1°$ North America
domain driven by ERA-interim reanalysis (Dee et al., 2011).

We use the ACT 5-second averaged CO_2 measurement dataset (Davis et al., 2018b) , which has a horizontal resolution approximately 500 m given the average aircraft velocity. MPAS simulated CO_2 fields are interpolated in time and space to match
each 5-second airborne data points. WRF-Chem simulated CO_2 fields are also interpolated to match the ACT 5-second data
point using the same approach as MPAS. CarbonTrack CO_2 used for the evaluation is obtained from CarbonTrack ObsPack
((Masarie et al., 2014)), which is the CT2019 posterior mole fraction interpolated to the ACT 5-second data points.

For each ACT flight day, CO_2 measurements from the two aircraft are combined if both are available, and their corresponding
modeled CO_2 values from MPAS, WRF-Chem, and CT2019 are combined in the same way. With the four seasons combined,
there are a total of 97 flight days (Pal and Davis, 2020), each one presented by an observation-model dataset consisted of
observed CO_2, modeled CO_2 from the three models, along with the time, latitude, longitude, and altitude of each observation
data point. Using the ACT maneuver flag dataset Pal et al. (2020), we further divide each flight day's data into two groups:
one for the boundary layer (BL) and another for he free troposphere (FT). RMSE and bias of the modeled CO_2 from the three
models (MPAS, WRF-Chem, and CT2019) are then calculated for each flight day, with the calculations for the BL and FT
carried out separately. In addition to the RMSE and bias, standard deviation is also calculated for the observed and modeled

CO_2 for assessing each model's representation of CO_2 spatial variability.

Using RMSE as an accuracy metric, we compare MPAS CO_2 simulation with WRF-Chem and CT2019 in Fig. 4. The figure shows that all three models have higher accuracy (lower RMSE) in FT than BL, which is most likely because flux errors impact

5   simulated CO_2 in BL more than in FT. The figure also shows that compared with WRF-Chem, MPAS has a similar magnitude of RMSE overall in both BL and FT, with some exception where substantial differences exist between the two models. Averaged over the 97 flight days, the mean RMSE is 4.49/1.85 ppm (BL/FT) for MPAS, and 4.91/1.71 ppm for WRF-Chem, indicating MPAS achieved a slightly higher accuracy than WRF-Chem in BL which maybe partially because the former has a higher horizontal resolution (15 km) than the latter (27 km). In free troposphere, WRF-Chem resulted in a slightly higher accu-

10 racy than MPAS maybe because that it applied meteorological nudging while MPAS did not. Compared with CT2019, MPAS simulations resulted in larger RMSE in the majority of flight days, and the differences in RMSE between the two models are large in BL than FT. Averaged over the 97 flight days, the mean RMSE for CT2019 is 3.36 ppm and 1.42 ppm in BL and FT respectively, which are substantially lower than MPAS (4.49 ppm/1.85 ppm in BL/FT).

15 Next we examine how well each model represents the CO_2 spatial variability (as measured by standard deviation). Fig. 5 shows the comparison of the standard deviation (σ) of the modeled and aircraft observed CO_2. The figure shows that the observed CO_2 has higher variability (σ) in BL than in FT (note that different scales are used for BL and FT plots). The figure also shows that the MPAS simulated CO_2 has larger σ than the observations in most of the flight days (Fig. 5(a). and (d)). In comparison, CT2019 CO_2 has substantially lower variability than the observations in the majority of the flight days (Fig. 5(c).

20 and (f)), especially in the boundary layer. Averaged over the 97 flight days, ACT airborne CO_2 observations has a mean σ of 3.53 ppm in BL, comparing to 4.27 ppm of MPAS, 4.63 ppm of WRF-Chem, and 2.23 ppm of CT2019.

The above model evaluation using airborne observations shows that the MPAS CO_2 transport model is capable of achieving a similar level of accuracy as 27 km resolution WRF-Chem simulation. Compared with the global inversion system CT2019,

25 although MPAS resulted in higher RMSEs, it achieved better estimations of the observed CO_2 spatial variability.

3.3.3   Model representation of CO_2 difference between warm and cold sectors

Through analyzing the ACT Summer 2016 campaign data, Pal et al. (2020) identified three consistent features in CO_2 mole fraction and proposed to use these features as transport model assessment metrics. The three features are the differences be-

30 tween the warm and cold sectors, the difference between the boundary layer and free troposphere, and the CO_2 enhancement bands in the vicinity of frontal boundaries. Here and in next two sections, we evaluate how MPAS simulated CO_2 represents the three features.

Using the ACT maneuver flag dataset (Pal et al., 2020), we identified flights that crossed a weather front and their associated warm and cold sectors. The CO_2 mole fraction statistics for the warm and cold sectors are calculated from the aircraft measurements and the modeled CO_2 by MPAS, WRF-Chem, and CT2019, respectively. The results are shown in Fig. 6, which summarizes the statistics of CO_2 mole fraction differences between the warm and cold sectors measured by 15 front-crossing

5   flights: 10 from the summer 2016 season and 5 from the winter 2017 season. The figure confirms that warm sector has higher average CO_2 mole fraction in the boundary layer than the cold sector during summer 2016 as reported by Pal et al. (2020). The figure also shows that the average CO_2 mole fraction in the warm sectors are lower than than the colder sectors in winter 2017, opposite to the summer 2016.

10   Fig. 6 also shows that MPAS simulated CO_2 well represents the difference between the warm and cold sectors well in all 15 cases. Table 4 lists the mean and standard deviation of the warm and cold sectors as calculated from the ACT measurements, MPAS, WRF-Chem, and CT2019. The table shows that the MPAS simulations are similar to WRF-Chem, and both tend to have larger CO_2 differences between the warm and cold sectors than CT2019. For instance, the 2016-08-24 case where the observed mean CO_2 difference between warm and cold sector is about 14 ppm, MPAS and WRF simulations resulted in 13.8

15   ppm and 7.8 ppm respectively, while CT2019 results in a 3.3 ppm difference. The above evaluation indicates that MPAS CO_2 model is capable of well representing the observed CO_2 difference between the warm and cold sectors, and its accuracy in this respect is similar to WRF-Chem and CT2019.

3.3.4   Model representation of CO_2 vertical difference

20   The second feature identified by Pal et al. (2020) is the vertical difference of CO_2 mole fraction between BL and FT. During ACT campaign season, two research aircraft (B200 and C130) took many vertical profile measurements during take off, landing, spiral up and down, and inline ascend and descend maneuvers (Pal, 2019). These profile observations characterize the vertical variation of atmospheric CO_2 mole fraction. From the vertical profile measurements taken during the summer 2016 season, Pal et al. (2020) calculated the mean CO_2 mole fraction in the boundary layer (BL) and free toposphere (FT), denoted

25   as $[CO_2]_{BL}$ and $[CO_2]_{FT}$ respectively. They further defined BL-to-FT CO_2 difference as $\Delta[CO_2] = [CO_2]_{BL} - [CO_2]_{FT}$. They found that $\Delta[CO_2]$ tend to be positive in the warm sector and negative in the cold sector. In this section, we evaluate how well MPAS represent the BL-to-FT CO_2 difference and compare its performance with WRF-Chem and CT2019.

Using the ACT maneuver flag dataset (Pal et al., 2020), we identified all vertical profiles taken during the four campaign

30   seasons, from which we selected profiles that meet two criteria: (1) a vertical profile must include at least 20 5-second measurements in the boundary layer and 20 measurements in the free troposphere; and (2) a vertical profile must extend at least 2 km in the vertical direction. These two criteria are used to ensure that the resulting $[CO_2]_{BL}$ and $[CO_2]_{BL}$ are statistically representative. A total of 199 qualified vertical profiles are identified from the four campaign seasons, including 72 from the summer 2016 season, 27 from winter 2017, 41 from fall 2017, and 59 from spring 2018. For each of the vertical profiles,

$\Delta[CO_2]$ is calculated for the aircraft CO_2 measurements, and the simulated CO_2 by MPAS, WRF-Chem, and CT2019. We compare $\Delta[CO_2]$ from the models with that from the observation to assess how each model represents the observed BL-to-FT CO_2 difference. Fig. 7 shows the comparisons grouped by the campaign seasons. The figure indicates a clear distinction in $\Delta[CO_2]$ between the summer 2016 and the other three seasons: There are substantial number of both positive and negative $\Delta[CO_2]$ in the summer 2016 season, but the vast majority cases in the rest of three campaign seasons have positive $\Delta[CO_2]$. The positive BL-to-FT CO_2 differences from the winter 2017 season measurements could be at least partially attributable to the lack of CO_2 draw-down during the non-growing season. In comparison, the fall 2017 and spring 2018 seasons have more mixed results probably because their partial overlap with the growing season. For the summer 2016 season, vertical profiles with negative $\Delta[CO_2]$ (lower mean CO_2 in BL than FT) suggest photosynthesis during the growing season, but those with positive $\Delta[CO_2]$ values are probably caused by the interaction between photosynthesis and frontal passage (Pal et al., 2020).

The comparison of $\Delta[CO_2]$ in Fig. 7 between the aircraft observations and the model simulations show how well the three models represent the BL-to-FT CO_2 difference. For instance, the figure indicates that MPAS represents the BL-to-FT difference more accurately during the fall 2017 seasons than the summer 2016 season. In comparison CT2019 represents BL-to-FT CO_2 difference more accurately during the summer 2015 season than the Fall 2017 season. The figure also show that while the comparisons between CT2019 and the aircraft observations have less scattering than MPAS and WRF-Chem, CT2019 also tend to underestimate the range of the BL-to-FT CO_2 differences, particularly during the spring 2018 season. To provide a quantitative evaluation, we calculated RMSE for each of the model-observation comparison of Fig. 7. In addition, the standard deviation of $\Delta[CO_2]$ is calculated for the observation and the three models for each season. The resulting statistics are summarized in Table 5 which shows that: MPAS has lower RMSEs than WRF-Chem in all but the summer 2016 season, and it has lower RMSEs than CT2019 for the winter and fall of 2017 but higher in the other two seasons. Regarding the standard deviations, MPAS compares with the observation better than WRF-Chem in all four season, and better than CT2019 in all but the summer 2016 season. In summary, the above model evaluation and comparison demonstrate that MPAS CO_2 transport model is capable of representing the aircraft observed CO_2 difference between boundary layer and free troposphere at least as accurately as WRF-Chem and CT2019.

3.3.5 Model representation of CO_2 enhancement at frontal boundaries

The third feature identified by Pal et al. (2020) in the summer 2016 aircraft measurements is the bands of enhanced CO_2 close to frontal boundaries in the boundary layer. They found these CO_2 enhancement bands are typically about 100 km wide and speculated that it would require a 20-km horizontal resolution model to effectively represent the feature. In this section, we identify the frontal boundary CO_2 enhancements in the four campaign seasons and examine how well they are represented by MPAS. For instance, Fig. 8 shows the MPAS simulated equivalent potential temperature (θ_e) and CO_2 mole fraction at 18:00 UTC 4 August 2016. The sharp boundary in θ_e indicates a surface cold front extending from southern Colorado northeastward to Wisconsin. Abrupt horizontal wind direction changes shown in Fig. S3 (supplement material) also indicate the cold front and

its southeastward movement. Meteorological measurements taken during the flight (not shown) confirm the cold front passage too. The B200 research aircraft crossed the cold front from southeast to northwest at about 400-500 meters above the ground between 17:15 UTC and 19:15 UTC, and its flight track and timing are marked on Fig. 8. The aircraft measurements show an approximately 20 ppm enhancement along the front boundary, which can be clearly identified in the MPAS simulated CO_2

5   mole fraction (lower panel of Fig. 8).

Using the same approach as Pal et al. (2020), a total of 48 front-crossing level-leg flight are identified from the four seasons (15 from Summer 2016, 5 from Winter 2017, 17 from Fall 2017, and 11 from Fall 2018). To evaluate how well MPAS represents the frontal boundary CO_2 enhancements and compare its performance with WRF-Chem and CT2019, CO_2 mole

10   fraction measured by the aircraft and simulated by the three models are plotted together for each of the identified front-crossing level-leg flight in Fig. 9. For each flight in the figure, the vertical dashed line marks the approximate time when the aircraft crossed the frontal boundary, and the associated warm and cold sectors are labeled on either side of the boundary. Examination of the aircraft observations (black lines) in the figure indicate that frontal boundary CO_2 enhancements can be identified in most of the flights but not all cases. For instance, there is not clearly identifiable CO_2 enhancement in the B200 flights on

15   2017-10-08 and 2018-04-23.

Fig. 9 shows that MPAS (red lines in the figure) has a varying degree of success in simulating the frontal boundary CO_2 enhancements: it represents both the timing and the magnitude of the enhancements very well in some cases (2017-10-28 and 2017-11-03 by B200), but results in substantial errors in either the timing (2016-08-12 B200) or the magnitude (2017-03-10

20   C130) in other cases. The figure also shows that the MPAS simulated CO_2 is more similar to WRF-Chem than CT2019: CT2019 tends to substantially underestimate the magnitude of CO_2 enhancement while MPAS and WRF-Chem tend to over-estimate.

To provide an quantitative comparison between the three models' accuracy regarding the frontal boundary CO_2 variation,

25   we calculated RMSE and standard deviation for each of the 48 level-leg flights shown in Fig. 9. For each flight, RMSE is calculated for each of the three models as compared with the aircraft observations, and standard deviation is calculated for both the models and aircraft observations. The resulting RMSEs from MPAS are compared with WRF-Chem and CT2019 in Fig. 10. The figure indicates that MPAS RMSEs in general are similar in magnitude to CT2019 and lower than WRF-Chem. Averaged over the 48 cases, the mean RMSE is 4.63 ppm for MPAS, 4.68 ppm for CT2019, and 5.86 ppm for WRF-Chem, indicating

30   MPAS perform as well as the other two models as measured by the RMSEs. We also assess how well the three models estimate the spatial variability of the frontal boundary CO_2 by comparing the standard deviation (σ) of the three models with the observations (Fig. 11). The figure shows that MPAS and WRF-Chem represent the spatial variability in the 48 level-leg flights better than CT2019 which substantially underestimates the variability in the majority of the cases. As horizontal resolution impacts a model's ability to represent small scale spatial variability (Agusti-Panareda et al., 2019), the coarser resolution of CT2019

($1° \times 1°$ over the North America) is likely the primary cause of its underestimation of the frontal boundary CO_2 variability.

3.4 Model evaluation using near-surface hourly CO_2 observations

The MPAS CO_2 transport model has been evaluated using the extensive high-resolution aircraft measurements from four ACT
5 campaign seasons. Considering that these aircraft measurements were all acquired during the day time hours over the eastern
United States, here we carry out further model evaluation using near-surface hourly CO_2 observations acquired by surface and
tower stations located across the globe. For this evaluation, we conducted another set of MPAS CO_2 simulations which cover
the month of January and July of 2014 using the same model domain and configurations as described in Sect. 3.1. As this is
the same time period that Agusti-Panareda et al. (2019) used for their IFS global CO_2 simulations, we can assess the MPAS
10 model performance through a comparison with the IFS simulations.

As with the simulations for the 2016-2018 ACT campaign seasons, we first evaluate the MPAS simulated horizontal wind
fields using radiosonde observations from 457 stations located around the globe (Fig. S3 of the supplement material). The
resulting statistics, including the RMSE of vector wind, RMSE of wind speed and wind direction, and the mean wind direction
15 difference are shown in Table 3. Compared with the IFS simulations by Agusti-Panareda et al. (2019) (their Fig. 4), the MPAS
simulated horizontal wind fields have larger errors in both January and July of 2014. For instance, the IFS 80 km resolution
simulation has a vector wind RMSE about 4.5 m/s at the 200 hPa level in January while MPAS results in 5.16 m/s at the same
pressure level.

20 We then compare MPAS simulated CO_2 with hourly measurements from 50 stations that were used for the IFS model
evaluation in Agusti-Panareda et al. (2019). The information of the 50 stations, including location, elevation, intake height,
and reference is listed Table 7. Like in Agusti-Panareda et al. (2019), only the highest intake level is used at towers that have
multiple intake heights. When multiple observations within an hour are available (such as those with 30-min or shorter time
interval), they are averaged to yield a single hourly value. For a given station this result in 744 (24×31) hourly measurements
25 per month at the maximum. Following Patra et al. (2008) and Agusti-Panareda et al. (2019), MPAS hourly outputs are horizon-
tally sampled by taking the nearest land cell to a given station. The resulting statistics (RMSE, bias, and STDE) for the MPAS
simulation covering the month of January 2014, along with their counterparts from the IFS 9 km and 80 km resolution simu-
lations (Agusti-Panareda et al., 2019), are listed in Table S1 of the supplement material. The table shows that RMSEs of the
MPAS simulated hourly CO_2 ranges from 0.36 ppm at the spo to 25.96 ppm at ssl station. In comparison, the IFS simulations
30 also resulted in a much lower RMSE at the spo than ssl, the latter of which has a RMSE of 5.83 ppm from 9 km resolution sim-
ulation and 23.99 ppm from the 80 km simulation. Agusti-Panareda et al. (2019) noted that the increasing horizontal resolution
improves model simulation accuracy the most at mountain stations. The Schauinsland station (ssl), located at the southwest
Germany with an elevation of 1205 meters above the means sea level, has considerable CO_2 variability because its vicinity to
biogenic and anthropogenic sources and sinks (Schmidt et al., 2003). This station is located in the 60-km resolution portion

of the MPAS 60-15km global domain, and the MPAS RMSE (25.96 ppm) at the station is closer to the IFS 80 km simulation (23.99ppm) than the 9km simulation (5.83 ppm), suggesting the influence of the model horizontal resolution. At this station, MPAS results in a positive bias of 21.34 ppm and IFS 80 km simulation has a positive bias of 18.72 ppm, meaning that both models substantially overestimate the hourly CO_2. An examination of the MPAS simulated hourly CO_2 (not shown) indicates

5   that the large bias is mostly caused by overestimation at the station during the nighttime hours. Such overestimation could be caused by a combination of errors in fluxes, vertical mixing, and large scale transport.

Finally, we compare RMSE and random error (STDE) of the MPAS simulation at the 46 stations with the IFS simulations in Fig. 12. The figure shows that MPAS has larger RMSE and STDE than the IFS 9 km simulation, but similar to the 80 km IFS

10   simulation. Similar model evaluation and comparison carried out for the month of July 2014 are shown in Table S2 (supplement material) and Fig. 13. Comparing with the January simulation, Fig. 13 shows that both MPAS and IFS have larger RMSEs in July, suggesting the impacts of large uncertainty in biospheric carbon fluxes during boreal summer. Fig. 13 also shows that the MPAS simulation has larger RMSE and STDE than the 9 km IFS simulation but similar to the 80 km IFS simulation, a similar pattern as in January.

4   Summary

This paper implemented CO_2 transport in the global variable-resolution model MPAS-A v6.3. The atmospheric CO_2 transport processes, including advection, vertical mixing, and convective transport, are implemented in the model. After the model development details are presented, simulation experiments designed for model evaluation are described. Two sets of simulations

20   over a 60-15 km variable-resolution global domains are conducted for model accuracy evaluation using an extensive aircraft measurements over the eastern United States and near-surface hourly measurements from surface and tower stations distributed across the globe. Meteorology initial conditions for these simulations are from the ERA-interim analysis (Dee et al., 2011), and CO_2 initial conditions and fluxes are from CT2019 posterior mole fraction and fluxes products (Jacobson et al., 2020). To keep model meteorological fields close to the analysis, meteorology re-initialization are applied at 24-hour interval throughout

25   the simulation periods. Global CO_2 mass conservation property is assessed by a continuous simulation without meteorology re-initialization and fluxes, and the results show that MPAS is capable of maintaining CO_2 mass conservation to the limit of machine precision. A 48-days simulation with meteorology re-initialization indicates that changes in dry air density during the re-initialization causes changes in global total CO_2 mass, and a scaling method applied after each re-initialization is able to reduce the global CO_2 mass variation to less than $\pm0.001\%$ of its initial value.

The accuracy of MPAS CO_2 transport is evaluated using the extensive high-resolution aircraft measurements from four ACT campaign seasons during 2016-2018. Compared with a 27 km resolution WRF-Chem simulation and CT2019 posterior CO_2 mole fraction, MPAS simulated CO_2 achieves a comparable level of accuracy (as measured by RMSE). Further evaluation

using three metrics proposed by Pal et al. (2020) shows that MPAS simulation is capable of representing the observed CO_2 features as accurately as the WRF-Chem simulation and CT2019.

5   A second set of MPAS simulations for the month of January and July of 2014 are evaluated using near-surface hourly CO_2 measurements from surface and tower stations across the global. The resulting statistic, including RMSE, random error, and bias, are compared with the ECWMF IFS 9km and 80 km resolution simulations over the same period conducted by Agusti-Panareda et al. (2019). The comparison indicates that RMSE and random error of the MPAS simulation is similar to the 80 km IFS simulation, but larger than the 9 km IFS simulation.

10   The model evaluations using the airborne and near-surface measurements, indicates that the newly developed MPAS CO_2 transport model is capable of achieving a comparable level of accuracy with the more established CO_2 modeling systems, including the regional model system WRF-Chem, the operational assimilation system CarbonTracker, and the lower resolution (80 km) simulation of ECWMF IFS global CO_2 modeling sytem. Although further improvements are expected, the MPAS CO_2 transport model has the potential to contribute to improving our knowledge of the atmospheric CO_2 transport and fluxes.

15   **Code and data availability**

Source code for MPAS-A CO_2 transport model v6.3 can be retrieved at https://doi.org/10.5281/zenodo.3976320 (Zheng, 2020). Source code for WRF-Chem v3.6 used in the manuscript can be obtained from NCAR website at http://www2.mmm.ucar.edu/wrf/users/download/get_source.html. Source code for IFS is only available subject to a licence agreement with ECMWF. ECMWF member-state weather services and their approved partners will get access granted. The
20   IFS source code without modules for assimilation and chemistry can be obtained for educational and academic purposes as part of the openIFS release (https:// software.ecmwf.int/wiki/display/OIFS/OpenIFS+Home). ACT-America in-situ Airborne CO_2 measurement data can be obtained at https://doi.org/10.3334/ORNLDAAC/1593. Surface and tower based CO_2 measurement data from ObsPack GLOBALVIEWplus v6.0 can be obtained from NOAA website https://esrl.noaa.gov/gmd/ccgg/obspack/data.php. CarbonTrack CO_2 flux and posterior mixing ratio data can be obtained from NOAA website
25   https://www.esrl.noaa.gov/gmd/ccgg/carbontracker/download.php.

Author contributions

TZ implemented the CO2 transport processes in MPAS v6.3. SF conducted the WRF 27km simulations. TZ, SF, KD, SP designed model evaluation using ACT-America aircraft measurements. TZ and JM designed the model evaluation using continuous in-situ tower measurements. TZ, SF, KD, SP analyzed the model representation of distinct CO2 spatial features observed
30   by the aircraft measurements. All authors contributed to writing and commenting on the paper.

Acknowledgment

We thank the MPAS development team for making their code available for the public; we thank NOAA CarbonTracker team for providing the CT2019 flux and mole fraction data; we thank ECWMF for the ERA-interim analysis data; we thank ObsPack data providers for the in-situ continuous CO2 measurement data. The model simulations were carried out on Michigan
5 State University High Performance Computing Center (HPCC). FS and KD were supported by the Atmospheric Carbon and Transport-America (ACT) Earth Venture Suborbital 2 project funded by NASA's Earth Science Division (Grant NNX15AG76G to Penn State), SP was supported by NASA Grant Number 80NSSC19K0730 and Texas Tech University start up research grant.

References

Agusti-Panareda, A., Massart, S., Chevallier, F., Boussetta, S., Balsamo, G., Beljaars, A., Ciais, P., Deutscher, N. M., Engelen, R., Jones, L., Kivi, R., Paris, J.-D., Peuch, V.-H., Sherlock, V., Vermeulen, A. T., Wennberg, P. O., and Wunch, D.: Forecasting global atmospheric CO_2, Atmospheric Chemistry and Physics, 14, 11 959–11 983, doi:10.5194/acp-14-11959-2014, https://www.atmos-chem-phys.net/14/11959/ 2014/, 2014.

Agusti-Panareda, A., Diamantakis, M., Bayona, V., Klappenbach, F., and Butz, A.: Improving the inter-hemispheric gradient of total column atmospheric CO_2 and CH_4 in simulations with the ECMWF semi-Lagrangian atmospheric global model, Geoscientific Model Development, 10, 1–18, doi:10.5194/gmd-10-1-2017, https://gmd.copernicus.org/articles/10/1/2017/, 2017.

Agusti-Panareda, A., Diamantakis, M., Massart, S., Chevallier, F., Munoz-Sabater, J., Barre, J., Curcoll, R., Engelen, R., Langerock, B., Law, R. M., Loh, Z., Anton Morgui, J., Parrington, M., Pench, V.-H., Ramonet, M., Roehl, C., Vermeulen, A. T., Warneke, T., and Wunch, D.: Modelling CO2 weather - why horizontal resolution matters, Atmospheric Chemistry and Physics, 19, 7347–7376, doi:10.5194/acp-19-7347-2019, 2019.

Andrews, A. E., Kofler, J. D., Trudeau, M. E., Williams, J. C., Neff, D. H., Masarie, K. A., Chao, D. Y., Kitzis, D. R., Novelli, P. C., Zhao, C. L., Dlugokencky, E. J., Lang, P. M., Crotwell, M. J., Fischer, M. L., Parker, M. J., Lee, J. T., Baumann, D. D., Desai, A. R., Stanier, C. O., De Wekker, S. F. J., Wolfe, D. E., Munger, J. W., and Tans, P. P.: CO_2, CO, and CH_4 measurements from tall towers in the NOAA Earth System Research Laboratory's Global Greenhouse Gas Reference Network: instrumentation, uncertainty analysis, and recommendations for future high-accuracy greenhouse gas monitoring efforts, Atmospheric Measurement Techniques, 7, 647–687, doi:10.5194/amt-7-647-2014, https://www.atmos-meas-tech.net/7/647/2014/, 2014.

Brunke, E., Labuschagne, C., Parker, B., Scheel, H., and Whittlestone, S.: Baseline air mass selection at Cape Point, South Africa: application of Rn-222 and other filter criteria to CO2, Atmospheric Environment, 38, 5693–5702, doi:10.1016/j.atmosenv.2004.04.024, 2004.

Chen, F. and Dudhia, J.: Coupling an advanced land surface-hydrology model with the Penn State-NCAR MM5 modeling system. Part I: Model implementation and sensitivity, Monthly Weather Review, 129, 569–585, doi:10.1175/1520-0493(2001)129<0569:CAALSH>2.0.CO;2, 2001.

Conway, T. J. and Thoning, K. W.: Short-term variations of atmospheric carbon dioxide at the South Pole, Anarctic Journal, pp. 236–238, 1990.

Davies, T.: Lateral boundary conditions for limited area models, Quarterly Journal of the Royal Meteorological Society, 140, 185–196, doi:10.1002/qj.2127, 2014.

Davis, K., Baier, B., Z., B., Bowman, K., Boyer, A., and Browell, E.: Atmospheric Carbon and Transport (ACT)- America: A multi-year airborne mission to study fluxes and transport of CO2 and CH4 across the eastern United States, american Geophysical Union Fall Meeting, 2018a.

Davis, K., Obland, M., Lin, B., Lauvaux, T., O'Dell, C., Meadows, B., Browell, E., DiGangi, J., Sweeney, C., McGill, M., Barrick, J., Nehrir, A., Yang, M., Bennett, J., Baier, B., Roiger, A., Pal, S., Gerken, T., Fried, A., Feng, S., Shrestha, R., Shook, M., Chen, G., Campbell, L., Barkley, Z., and Pauly, R.: ACT-America: L3 Merged In Situ Atmospheric Trace Gases and Flask Data, Eastern USA, doi:10.3334/ORNLDAAC/1593, https://daac.ornl.gov/cgi-bin/dsviewer.pl?ds_id=1593, 2018b.

Dee, D. P., Uppala, S. M., Simmons, A. J., Berrisford, P., Poli, P., Kobayashi, S., Andrae, U., Balmaseda, M. A., Balsamo, G., Bauer, P., Bechtold, P., Beljaars, A. C. M., van de Berg, L., Bidlot, J., Bormann, N., Delsol, C., Dragani, R., Fuentes, M., Geer, A. J., Haimberger, L., Healy, S. B., Hersbach, H., Holm, E. V., Isaksen, L., Kallberg, P., Koehler, M., Matricardi, M., McNally, A. P., Monge-Sanz,

B. M., Morcrette, J. J., Park, B. K., Peubey, C., de Rosnay, P., Tavolato, C., Thepaut, J. N., and Vitart, F.: The ERA-Interim reanalysis: configuration and performance of the data assimilation system, Quarterly Journal of the Royal Meteorological Society,, 137, 553–597, doi:10.1002/qj.828, 2011.

Diaz-Isaac, L. I., Lauvaux, T., and Davis, K. J.: Impact of physical parameterizations and initial conditions on simulated atmospheric transport and CO2 mole fractions in the US Midwest, Atmospheric Chemistry and Physics, 18, 14 813–14 835, doi:10.5194/acp-18-14813-2018, 2018.

Diaz-Isaac, L. I., Lauvaux, T., Bocquet, M., and Davis, K. J.: Calibration of a multi-physics ensemble for estimating the uncertainty of a greenhouse gas atmospheric transport model, Atmospheric Chemistry and Physics, 19, 5695–5718, doi:10.5194/acp-19-5695-2019, 2019.

Feng, S., Lauvaux, T., Barkley, Z. R, D. k. J., Butler, M. B., Deng, A., Gaudet, B., and D., S.: Full WRF-Chem output in support of the NASA Atmospheric Carbon and Transport (ACT)-America project (7/1/2016 – 7/31/2019). The Pennsylvania State University Data Commons, University Park, Pennsylvania, USA, doi:10.26208/49kd-b637, https://doi.org/10.26208/49kd-b637, 2020.

Feng, S., Lauvaux, T., Newman, S., Rao, P., Ahmadov, R., Deng, A., Diaz-Isaac, L. I., Duren, R. M., Fischer, M. L., Gerbig, C., Gurney, K. R., Huang, J., Jeong, S., Li, Z., Miller, C. E., O'Keeffe, D., Patarasuk, R., Sander, S. P., Song, Y., Wong, K. W., and Yung, Y. L.: Los Angeles megacity: a high-resolution land-atmosphere modelling system for urban CO_2 emissions, Atmospheric Chemistry and Physics, 16, 9019–9045, doi:10.5194/acp-16-9019-2016, 2016.

Feng, S., Lauvaux, T., Davis, K. J., Keller, K., Zhou, Y., Williams, C., Schuh, A. E., Liu, J., and Baker, I.: Seasonal Characteristics of Model Uncertainties From Biogenic Fluxes, Transport, and Large-Scale Boundary Inflow in Atmospheric CO2 Simulations Over North America, Journal of Geophysical Research-Atmospheres, 124, 14 325–14 346, doi:10.1029/2019JD031165, 2019.

Francey, R. J., Steele, L. P., Spencer, D. A., Langenfelds, R. L., Law, R. M., Krummel, P. B., Fraser, P. J., Etheridge, D. M., Derek, N., Coram, S. A., Cooper, L. N., Allison, C. E., Porter, L., and Baly, S.: The CSIRO (Australia) measurement of greenhouse gases in the global atmosphere, report of the 11th WMO/IAEA Meeting of Experts on Carbon Dioxide Concentration and Related Tracer Measurement Techniques, Tokyo, Japan, September 2001, edited by: Toru, S. and Kazuto, S., World Meteorological Organization Global Atmosphere Watch, 2003.

Fritsch, J. M. and Chappell, C. F.: Numerical prediction of convectively driven mesoscale pressure systems. Part I: convective parameterization, Journal of the Atmospheric Sciences, 37, 1722–1733, doi:10.1175/1520-0469(1980)037<1722:NPOCDM>2.0.CO;2, 1980.

Gaudry, A., Monfray, P., Polian, G., Bonsang, G., Ardouin, B., Jegou, A., and Lambert, G.: Nonseasonnal variations of atmospheric CO2 concentrations at Amsterdam Island, Tellus Series B-Chemical and Physical Meteorology, 43, 136–143, doi:10.1034/j.1600-0889.1991.00008.x, 1991.

Gerbig, C., Körner, S., and Lin, J. C.: Vertical mixing in atmospheric tracer transport models: error characterization and propagation, Atmospheric Chemistry and Physics, 8, 591–602, doi:10.5194/acp-8-591-2008, 2008.

Gerbig, C., Dolman, A. J., and Heimann, M.: On observational and modelling strategies targeted at regional carbon exchange over continents, Biogeosciences, 6, 1949–1959, doi:10.5194/bg-6-1949-2009, 2009.

Gockede, M., Turner, D. P., Michalak, A. M., Vickers, D., and Law, B. E.: Sensitivity of a subregional scale atmospheric inverse CO2 modeling framework to boundary conditions, Journal of Geophysical Research, 115, doi:10.1029/2010JD014443, 2010.

Golaz, J.-C., Caldwell, P. M., Van Roekel, L. P., Petersen, M. R., Tang, Q., Wolfe, J. D., and et al.: The DOE E3SM Coupled Model Version 1: Overview and Evaluation at Standard Resolution, Journal of Advances in Modeling Earth Systems, 11, 2089–2129, doi:10.1029/2018MS001603, 2019.

Gomez-Pelaez, A. J. and Ramos, R.: Improvements in the Carbon Dioxide and Methane Continuous Measurement Programs at Izana Global
GAW Station (Spain) during 2007–2009, in: GAW report (No. 194) of the 15th WMO/IAEA Meeting of Experts on Carbon Dioxide,
Other Greenhouse Gases, and Related Tracer Measurement Techniques (Jena, Germany; 7–10 September 2009), edited by: Brand, W. A.,
World Meteorological Organization (TD No. 1553), 2005.

5 Grell, G., Freitas, S. R., Stuefer, M., and Fast, J.: Inclusion of biomass burning in WRF-Chem: impact of wildfires on weather forecasts,
Atmospheric Chemistry and Physics, 11, 5289–5303, doi:10.5194/acp-11-5289-2011, 2011.

Halter, B., Harris, J., and Conway, T.: Component signals in the record of atmospheric carbon dioxide concentration at American Samoa,
Journal of Geophysical Research-Atmospheres, 93, 15 914–15 918, doi:10.1029/JD093iD12p15914, 1988.

Haszpra, L., Barcza, Z., Bakwin, P., Berger, B., Davis, K., and Weidinger, T.: Measuring system for the long-term moni-
10 toring of biosphere/atmosphere exchange of carbon dioxide, Journal of Geophysical Research-Atmospheres, 106, 3057–3069,
doi:10.1029/2000JD900600, 2001.

Hatakka, J., Aalto, T., Aaltonen, V., Aurela, M., Hakola, H., Komppula, M., Laurila, T., Lihavainen, H., Paatero, J., Salminen, K., and
Viisanen, Y.: Overview of the atmospheric research activities and results at Pallas GAW station, Boreal Environment Research, 8, 365–
383, 2003.

15 Hersbach, H., Bell, B., Berrisford, P., Hirahara, S., Horanyi, A., Munoz-Sabater, J., Nicolas, J., Peubey, C., Radu, R., Schepers, D., Simmons,
A., Soci, C., Abdalla, S., Abellan, X., Balsamo, G., Bechtold, P., Biavati, G., Bidlot, J., Bonavita, M., De Chiara, G., Dahlgren, P., Dee,
D., Diamantakis, M., Dragani, R., Flemming, J., Forbes, R., Fuentes, M., Geer, A., Haimberger, L., Healy, S., Hogan, R. J., Holm, E.,
Janiskova, M., Keeley, S., Laloyaux, P., Lopez, P., Lupu, C., Radnoti, G., de Rosnay, P., Rozum, I., Vamborg, F., Villaume, S., and Thepaut,
J.-N.: The ERA5 global reanalysis, Quaterly Journal of the Royal Meteorological Society, doi:10.1002/qj.3803.

20 Hong, S., Dudhia, J., and Chen, S.: A revised approach to ice microphysical processes for the bulk parameterization of clouds and precipita-
tion, Monthly Weather Review, 132, 103–120, doi:10.1175/1520-0493(2004)132<0103:ARATIM>2.0.CO;2, 2004.

Hong, S.-Y. and Lim, J.: Journal of the Korean Meteorological Society, 42, 29–151, 2006.

Hong, S.-Y., Noh, Y., and Dudhia, J.: A new vertical diffusion package with an explicit treatment of entrainment processes, Monthly Weather
Review, 134, 2318–2341, doi:10.1175/MWR3199.1, 2006.

25 Hu, L., Andrews, A. E., Thoning, K. W., Sweeney, C., Miller, J. B., Michalak, A. M., Dlugokencky, E., Tans, P. P., Shiga, Y. P., Mountain,
M., Nehrkorn, T., Montzka, S. A., McKain, K., Kofler, J., Trudeau, M., Michel, S. E., Biraud, S. C., Fischer, M. L., Worthy, D. E. J.,
Vaughn, B. H., White, J. W. C., Yadav, V., Basu, S., and van der Velde, I. R.: Enhanced North American carbon uptake associated with El
Niño, Science Advances, 5, doi:10.1126/sciadv.aaw0076, 2019.

Iacono, M. J., Delamere, J. S., Mlawer, E. J., Shephard, M. W., Clough, S. A., and Collins, W. D.: Radiative forcing by long-
30 lived greenhouse gases: Calculations with the AER radiative transfer models, Journal of Geophysical Research-Atmospheres, 113,
doi:10.1029/2008JD009944, 2008.

Jacobson, A. R., Fletcher, S. E. M., Gruber, N., Sarmiento, J. L., and Gloor, M.: A joint atmosphere-ocean inversion for surface fluxes of
carbon dioxide: 1. Methods and global-scale fluxes, Global Biogeochemical Cycles, 21, doi:10.1029/2006GB002703, gB1019, 2007.

Jacobson, A. R., Schuldt, K. N., Miller, J. B., Oda, T., Tans, P., Arlyn Andrews, Mund, J., Ott, L., Collatz, G. J., Aalto, T., Afshar, S., Aikin,
35 K., Aoki, S., Apadula, F., Baier, B., Bergamaschi, P., Beyersdorf, A., Biraud, S. C., Bollenbacher, A., Bowling, D., Brailsford, G., Abshire,
J. B., Chen, G., Huilin Chen, Lukasz Chmura, Sites Climadat, Colomb, A., Conil, S., Cox, A., Cristofanelli, P., Cuevas, E., Curcoll, R.,
Sloop, C. D., Davis, K., Wekker, S. D., Delmotte, M., DiGangi, J. P., Dlugokencky, E., Ehleringer, J., Elkins, J. W., Emmenegger, L.,
Fischer, M. L., Forster, G., Frumau, A., Galkowski, M., Gatti, L. V., Gloor, E., Griffis, T., Hammer, S., Haszpra, L., Hatakka, J., Heliasz,

M., Hensen, A., Hermanssen, O., Hintsa, E., Holst, J., Jaffe, D., Karion, A., Kawa, S. R., Keeling, R., Keronen, P., Kolari, P., Kominkova, K., Kort, E., Krummel, P., Kubistin, D., Labuschagne, C., Langenfelds, R., Laurent, O., Laurila, T., Lauvaux, T., Law, B., Lee, J., Lehner, I., Leuenberger, M., Levin, I., Levula, J., Lin, J., Lindauer, M., Loh, Z., Lopez, M., Myhre, C. L., Machida, T., Mammarella, I., Manca, G., Manning, A., Manning, A., Marek, M. V., Marklund, P., Martin, M. Y., Matsueda, H., McKain, K., Meijer, H., Meinhardt, F., Miles, N., Miller, C. E., Mölder, M., Montzka, S., Moore, F., Josep-Anton Morgui, Morimoto, S., Munger, B., Jaroslaw Necki, Newman, S., Nichol, S., Niwa, Y., O'Doherty, S., Mikaell Ottosson-Löfvenius, Paplawsky, B., Peischl, J., Peltola, O., Jean-Marc Pichon, Piper, S., Plass-Dölmer, C., Ramonet, M., Reyes-Sanchez, E., Richardson, S., Riris, H., Ryerson, T., Saito, K., Sargent, M., Sasakawa, M., Sawa, Y., Say, D., Scheeren, B., Schmidt, M., Schmidt, A., Schumacher, M., Shepson, P., Shook, M., Stanley, K., Steinbacher, M., Stephens, B., Sweeney, C., Thoning, K., Torn, M., Turnbull, J., Tørseth, K., Bulk, P. V. D., Laan-Luijkx, I. T. V. D., Dinther, D. V., Vermeulen, A., Viner, B., Vitkova, G., Walker, S., Weyrauch, D., Wofsy, S., Worthy, D., Dickon Young, and Miroslaw Zimnoch: CarbonTracker CT2019, doi:10.25925/39M3-6069, https://www.esrl.noaa.gov/gmd/ccgg/carbontracker/CT2019/, 2020.

Kain, J. S.: The Kain–Fritsch Convective Parameterization: An Update, Journal of Applied Meteorology, 43, 170–181, doi:10.1175/1520-0450(2004)043<0170:TKCPAU>2.0.CO;2, 2004.

Kain, J. S. and Fritsch, J. M.: A one-dimensional entraining detraining plume model and its application in convective parameterization, Journal of the Atmospheric Sciences, 47, 2784–2802, doi:10.1175/1520-0469(1990)047<2784:AODEPM>2.0.CO;2, 1990.

Krol, M., Houweling, S., Bregman, B., van den Broek, M., Segers, A., van Velthoven, P., Peters, W., Dentener, F., and Bergamaschi, P.: The two-way nested global chemistry-transport zoom model TM5: algorithm and applications, Atmospheric Chemistry and Physics, 5, 417–432, doi:10.5194/acp-5-417-2005, 2005.

Lauvaux, T. and Davis, K. J.: Planetary boundary layer errors in mesoscale inversions of column-integrated CO_2 measurements, Journal of Geophysical Research-Atmospheres, 119, 490–508, doi:10.1002/2013JD020175, 2014.

Lauvaux, T., Schuh, A. E., Uliasz, M., Richardson, S., Miles, N., Andrews, A. E., Sweeney, C., Diaz, L. I., Martins, D., Shepson, P. B., and Davis, K. J.: Constraining the CO_2 budget of the corn belt: exploring uncertainties from the assumptions in a mesoscale inverse system, Atmospheric Chemistry and Physics, 12, 337–354, doi:10.5194/acp-12-337-2012, https://www.atmos-chem-phys.net/12/337/2012/, 2012.

Loh, Z. M., Law, R. M., Ziehn, T., van der Schoot M. V., Krummel, P. B., Steele, L. P., Etheridge, D. M., Spencer, D. A., Gregory, R. L., Langenfelds, R. L., Stavert, A. R., and Thornton, D. P.: The Australian Greenhouse Gas Observation Network: Current status and vision for the future. 10th International Carbon Dioxide Conference (ICDC10),21–25 August 2017,Interlaken, Switzerland, http://www.icdc10.unibe.ch/unibe/portal/fak_naturwis/micro_icdc10/content/e342182/e604227/e604229/files623284/Loh_Zoe.pdf, 2017.

Lopez, M., Schmidt, M., Ramonet, M., Bonne, J.-L., Colomb, A., Kazan, V., Laj, P., and Pichon, J.-M.: Three years of semicontinuous greenhouse gas measurements at the Puy de Dôme station (central France), Atmospheric Measurement Techniques, 8, 3941–3958, doi:10.5194/amt-8-3941-2015, 2015.

Louis, J. F.: A parametric model of vertical eddy flux in the atmosphere, Boundary Layer Meteorology, 17, 187–202, 1979.

Masarie, K. A., Peters, W., Jacobson, A. R., and Tans, P. P.: ObsPack: a framework for the preparation, delivery, and attribution of atmospheric greenhouse gas measurements, Earth System Science Data, 6, 375–384, doi:10.5194/essd-6-375-2014, 2014.

Michaelis, A. C., Lackmann, G. M., and Robinson, W. A.: Evaluation of a unique approach to high-resolution climate modeling using the Model for Prediction Across Scales – Atmosphere (MPAS-A) version 5.1, Geoscientific Model Development, 12, 3725–3743, doi:10.5194/gmd-12-3725-2019, 2019.

Morgui, J. A., Agueda, A., Batet, O.and Curcoll, R., Ealo, M., G. C., Occhipinti, P., Sanchez-Garcia, L., Arias, R., and Rodo, X.: ClimaDat: A long-term network to study at different scales climatic processes and interactions between climatic compartments, Geophys. Res. Abstr., EGU13-10265, EGU General Assembly 2013, Vienna, Austria, 2013, 2013.

Necki, J., Schmidt, M., Rozanski, K., Zimnoch, M., Korus, A., Lasa, J., Graul, R., and Levin, I.: Six-year record of atmospheric carbon dioxide and methane at a high-altitude mountain site in Poland, Tellus Series B-Chemical and Physical Meteorology, 55, 94–104, doi:10.1034/j.1600-0889.2003.01446.x, 2003.

Noh, Y., Cheon, W., Hong, S., and Raasch, S.: Improvement of the K-profile model for the planetary boundary layer based on large eddy simulation data, Boundary Layer Meteorology, 107, 401–427, doi:10.1023/A:1022146015946, 2003.

Pal, S.: CT-America: Profile-based Planetary Boundary Layer Heights, Eastern USA. ORNL DAAC, Oak Ridge, Tennessee, USA, doi:10.3334/ORNLDAAC/1706, 2019.

Pal, S. and Davis, K.: ACT-America Field Campaign Catalogue. ORNL DAAC, Oak Ridge, Tennessee, USA., https://actamerica.ornl.gov/campaigns.html, 2020.

Pal, S., J., D. K., Lauvaux, T., B. E. V., Gaudet, B. J., and Stauffer, D.: Observations of Greenhouse Gas Changes Across Summer Frontal Boundaries in the Eastern United States, Journal of Geophysical Research -Atmospheres, 125, doi:10.1029/2019JD030526, 2020.

Patra, P. K., Law, R. M., Peters, W., Roedenbeck, C., Takigawa, M., Aulagnier, C., Baker, I., Bergmann, D. J., Bousquet, P., Brandt, J., Bruhwiler, L., Cameron-Smith, P. J., Christensen, J. H., Delage, F., Denning, A. S., Fan, S., Geels, C., Houweling, S., Imasu, R., Karstens, U., Kawa, S. R., Kleist, J., Krol, M. C., Lin, S. J., Lokupitiya, R., Maki, T., Maksyutov, S., Niwa, Y., Onishi, R., Parazoo, N., Pieterse, G., Rivier, L., Satoh, M., Serrar, S., Taguchi, S., Vautard, R., Vermeulen, A. T., and Zhu, Z.: TransCom model simulations of hourly atmospheric CO2: Analysis of synoptic-scale variations for the period 2002-2003, Global Biogeochemical Cycles, 22, doi:10.1029/2007GB003081, gB4013, 2008.

Peterson, J., Komhyr, W., Waterman, L., Gammon, R., Thoning, K., and Conway, T.: Atmospheric CO_2 variations at Barrow, Alaska,1973-1982, Journal of Atmosphere Chemistry, 4, 491–510, doi:10.1007/BF00053848, 1986.

Pillai, D., Gerbig, C., Kretschmer, R., Beck, V., Karstens, U., Neininger, B., and Heimann, M.: Comparing Lagrangian and Eulerian models for CO_2 transport – a step towards Bayesian inverse modeling using WRF/STILT-VPRM, Atmospheric Chemistry and Physics, 12, 8979–8991, doi:10.5194/acp-12-8979-2012, 2012.

Polavarapu, S. M., Neish, M., Tanguay, M., Girard, C., de Grandpré, J., Semeniuk, K., Gravel, S., Ren, S., Roche, S., Chan, D., and Strong, K.: Greenhouse gas simulations with a coupled meteorological and transport model: the predictability of CO_2, Atmospheric Chemistry and Physics, 16, 12 005–12 038, doi:10.5194/acp-16-12005-2016, 2016.

Putman, W. M. and Lin, S.-H.: Finite-volume transport on various cubed-sphere grids, JOURNAL OF COMPUTATIONAL PHYSICS, 227, 55–78, doi:10.1016/j.jcp.2007.07.022, 2007.

Ramonet, M., Ciais, P., Aalto, T., Aulagnier, C., Chevallier, F., Cipriano, D., Conway, T. J., Haszpra, L., Kazan, V., Meinhardt, F., Paris, J.-D., Schmidt, M., Simmonds, P., Xueref-Remy, I., and Necki, J. N.: A recent build-up of atmospheric CO2 over Europe. Part 1: observed signals and possible explanations, Tellus Series B-Chemical and Physical Meteorology, 62, 1–13, doi:10.1111/j.1600-0889.2009.00442.x, 2010.

Rayner, P. J., Michalak, A. M., and Chevallier, F.: Fundamentals of data assimilation applied to biogeochemistry, Atmospheric Chemistry and Physics, 19, 13 911–13 932, doi:10.5194/acp-19-13911-2019, 2019.

Ringler, T., Ju, L., and Gunzburger, M.: A multiresolution method for climate system modeling: application of spherical centroidal Voronoi tessellations, Ocean Dynamics, 58, 475–498, doi:10.1007/s10236-008-0157-2, 2008.

Ringler, T. D., Thuburn, J., Klemp, J. B., and Skamarock, W. C.: A unified approach to energy conservation and potential vorticity dynamics for arbitrarily-structured C-grids, Journal of Computational Physics, 229, 3065–3090, doi:10.1016/j.jcp.2009.12.007, 2010.

Rozanski, K., Necki, J., Chmura, L., Sliwka, I., Zimnoch, M., Bielewski, J., Galkowski, M., Bartyzel, J., and Rosiek, J.: Anthropogenic changes of CO2, CH4, N2O, CFCl3, CF2Cl2, CCl2FCClF2, CHCl3, CH3CCl3, CCl4, SF6 and SF5CF3 mixing ratios in the atmosphere over southern Poland, Geological Quarterly, 58, 673–684, doi:10.7306/gq.1163, 2014.

Sarrat, C., Noilhan, J., Lacarrere, P., Donier, S., Lac, C., Calvet, J. C., Dolman, A. J., Gerbig, C., Neininger, B., Ciais, P., Paris, J. D., Boumard, F., Ramonet, M., and Butet, A.: Atmospheric CO2 modeling at the regional scale: Application to the CarboEurope Regional Experiment, Journal of Geophysical Research-Atmospheres, 112, doi:10.1029/2006JD008107, 2007.

Schibig, M. F., Steinbacher, M., Buchmann, B., van der Laan-Luijkx, I. T., van der Laan, S., Ranjan, S., and Leuenberger, M. C.: Comparison of continuous in situ CO_2 observations at Jungfraujoch using two different measurement techniques, Atmospheric Measurement Techniques, 8, 57–68, doi:10.5194/amt-8-57-2015, 2015.

Schmidt, M., Graul, R., Sartorius, H., and Levin, I.: The Schauinsland CO2 record: 30 years of continental observations and their implications for the variability of the European CO2 budget, Journal of Geophysical Research-Atmospheres, 108, doi:10.1029/2002JD003085, 2003.

Schuh, A. E., Lauvaux, T., West, T. O., Denning, A. S., Davis, K. J., Miles, N., Richardson, S., Uliasz, M., Lokupitiya, E., Cooley, D., Andrews, A., and Ogle, S.: Evaluating atmospheric CO2 inversions at multiple scales over a highly inventoried agricultural landscape, Global Change Biology, 19, 1424–1439, doi:10.1111/gcb.12141, 2013.

Schuh, A. E., Jacobson, A. R., Basu, S., Weir, B., Baker, D., Bowman, K., Chevallier, F., Crowell, S., Davis, K. J., Deng, F., Denning, S., Feng, L., Jones, D., Liu, J., and Palmer, I, P.: Quantifying the Impact of Atmospheric Transport Uncertainty on CO2 Surface Flux Estimates, Global Biogeochemical Cycles, 33, 484–500, doi:10.1029/2018GB006086, 2019.

Skamarock, W., Klemp, J., Dudhia, J., Gill, D., Barker, D., Duda, M., Huang, X., Wang, W., and Powers, J.: A description of the Advanced Research WRF version 3, NCAR Tech Note NCAR/TN-475+STR, 2008.

Skamarock, W. C. and Gassmann, A.: Conservative Transport Schemes for Spherical Geodesic Grids: High-Order Flux Operators for ODE-Based Time Integration, Monthly Weather Review, 139, 2962–2975, doi:10.1175/MWR-D-10-05056.1, 2011.

Skamarock, W. C., Klemp, J. B., Duda, M. G., Fowler, L. D., Park, S.-H., and Ringler, T. D.: A Multiscale Nonhydrostatic Atmospheric Model Using Centroidal Voronoi Tesselations and C-Grid Staggering, Monthly Weather Review, 140, 3090–3105, doi:10.1175/MWR-D-11-00215.1, 2012.

Stephens, B. B., Miles, N. L., Richardson, S. J., Watt, A. S., and Davis, K. J.: Atmospheric CO_2 monitoring with single-cell NDIR-based analyzers, Atmospheric Measurement Techniques, 4, 2737–2748, doi:10.5194/amt-4-2737-2011, https://www.atmos-meas-tech.net/4/2737/2011/, 2011.

Thoning, K., Tans, P., and Komhyr, W.: Atmospheric carbon dioxide at Mauna Loa Observatory, 2. Analysis of the NOAA/GMCC data, 1974-1985, Journal of Geophysical Research-Atmospheres, 94, 8549–8565, doi:10.1029/JD094iD06p08549, 1989.

Thuburn, J.: Rossby wave dispersion on the C-grid, Atmospheric Science Letters, 8, 37–42, doi:10.1002/asl.148, 2007.

Tsutsumi, Y., Matsueda, H., and Nishioka, S.: Consistency of the CO2 primary standards in JMA, 12th WMO/IAEA meeting of experts on carbon dioxide concentration and related tracers measurement techniques (Toronto, Canada, 15– 18 September 2003), Global Atmosphere Watch Report No. 161 (WMO/TD-No.1275), 2005.

Vermeulen, A. T., Hensen, A., Popa, M. E., van den Bulk, W. C. M., and Jongejan, P. A. C.: Greenhouse gas observations from Cabauw Tall Tower (1992–2010), Atmospheric Measurement Techniques, 4, 617–644, doi:10.5194/amt-4-617-2011, https://www.atmos-meas-tech.net/4/617/2011/, 2011.

Walko, R. L. and Avissar, R.: The Ocean-Land-Atmosphere Model (OLAM). Part I: Shallow-Water Tests, Monthly Weather Review, 136, 4033–4044, doi:10.1175/2008MWR2522.1, 2008a.

Walko, R. L. and Avissar, R.: The Ocean-Land-Atmosphere Model (OLAM). Part II: Formulation and Tests of the Nonhydrostatic Dynamic Core, Monthly Weather Review, 136, 4045–4062, doi:10.1175/2008MWR2523.1, 2008b.

5 Wilson, P.: Insight into the Carbon Cycle from Continuous Measurements of Oxygen and Carbon Dioxide at Weybourne Atmospheric Observatory, UK,, PhD thesis, University of East Anglia, Norwich, UK, 2013.

Worthy, D., Higuchi, K., and Chan, D.: North American influence on atmospheric carbon dioxide data collected at Sable Island, Canada, Tellus Series B-Chemical anD Physical Meteorology, 55, 105–114, doi:10.1034/j.1600-0889.2003.00051.x, 2003.

Zheng, T.: MPAS CO2 transport model, doi:10.5281/zenodo.3976320, https://doi.org/10.5281/zenodo.3976320, 2020.

10 Zheng, T., Nassar, R., and Baxter, M.: Estimating power plant CO_2 emission using OCO-2 XCO_2 and high resolution WRF-Chem simulations, Environmental Research Letters, 14, doi:10.1088/1748-9326/ab25ae, 2019.

Zheng, T., French, N. H. F., and Baxter, M.: Development of the WRF-CO_2 4D-Var assimilation system v1.0, Geoscientific Model Development, 11, 1725–1752, doi:10.5194/gmd-11-1725-2018, 2018.
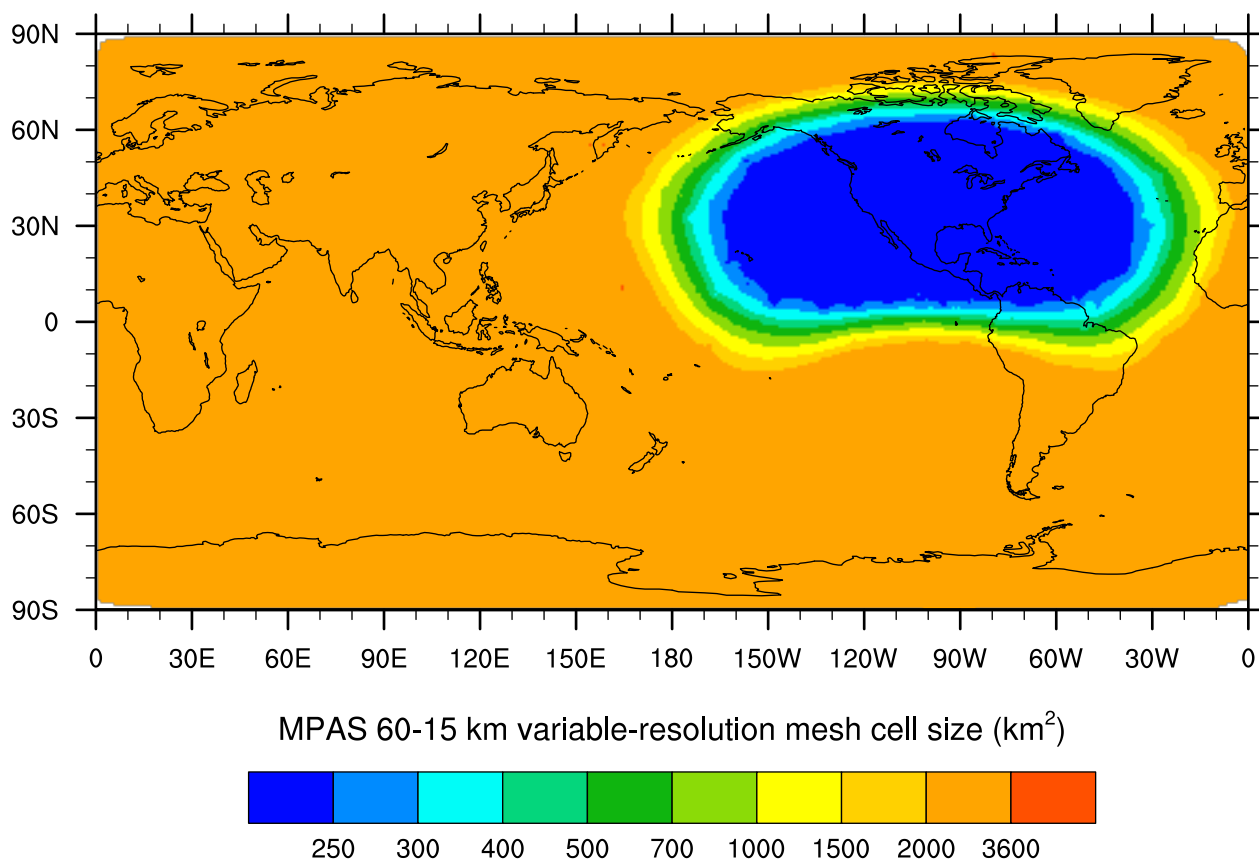
Figure 1. Variable-resolution 60-15 km global domain for MPAS CO_2 simulations conducted for model evaluation using aircraft and near-surface CO_2 observations. The highest resolution (15 km) grid covering the most of the North America has cell size less than 250 km^2. The cell sizes (represented by color) gradually increase to about 3,600 km^2 for the rest of the global domain.

Number of hours since the start of simulation
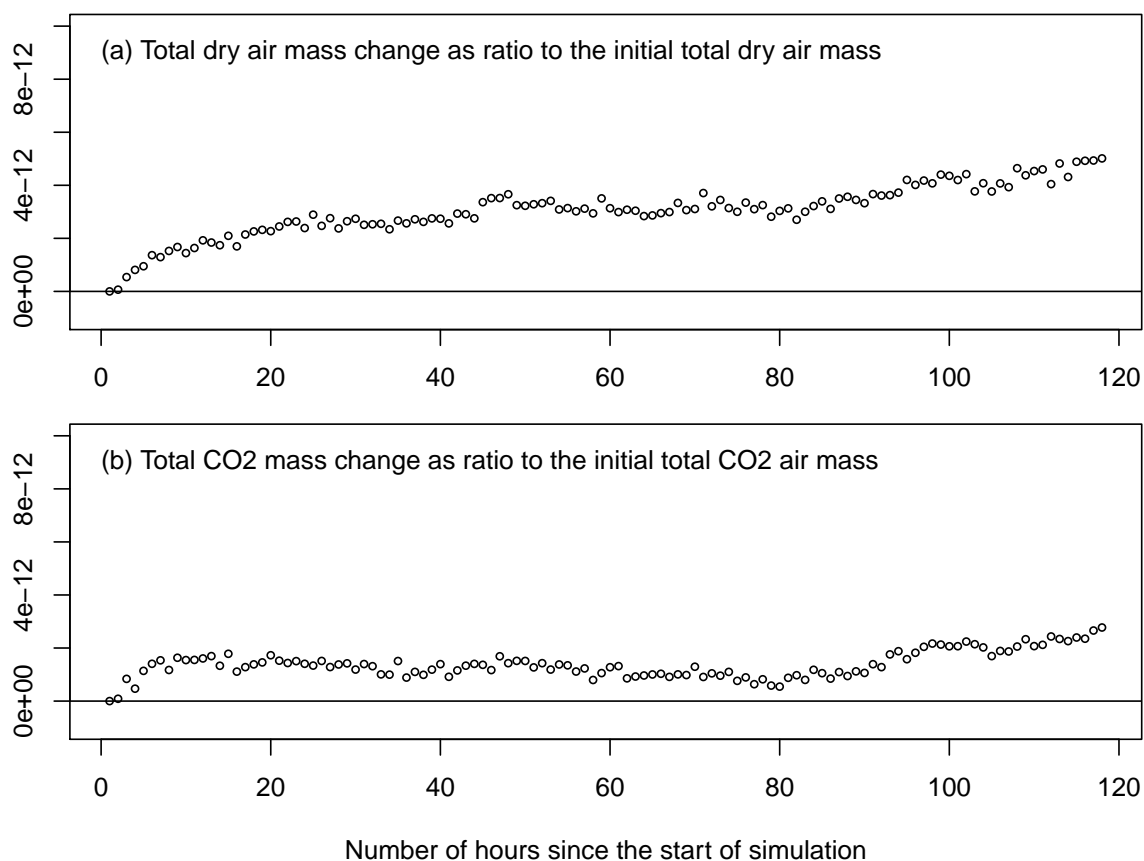
Figure 2. Variation of total dry air mass (a) and total CO_2 mass (b) as the ratio to their respective starting values during a 120-hour continuous MPAS simulation without meteorology re-initialization. The X-axis represents the number of hours after the start of the simulation, and the Y-axis the ratio of the total mass change to the starting values.

Days since the start of simulation (15 July 2016 00:00 UTC)
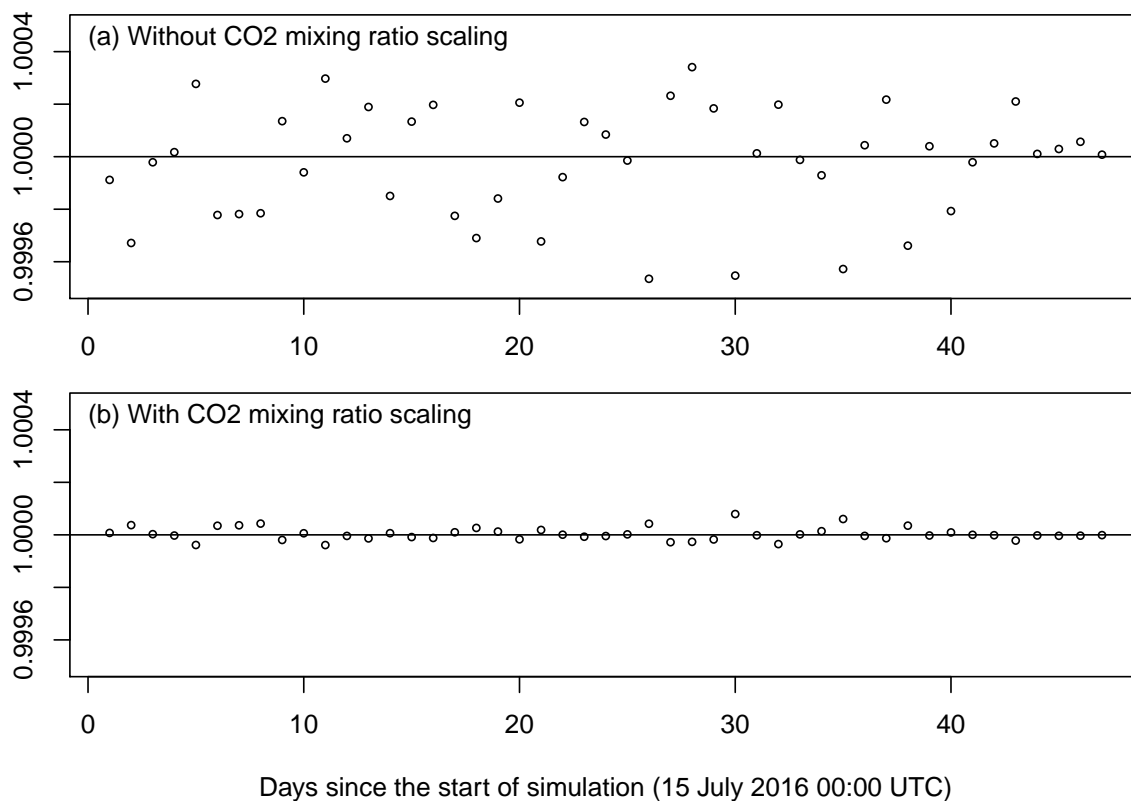
Figure 3. Variation of total CO_2 mass as the ratio to its starting value during a 48-day MPAS simulation with meteorology re-initializations at 24-hour intervals. The top figure is from the simulation without applying CO_2 mixing ratio scaling as described in Sect. 3.2.2, and the bottom figure is from the simulation with the scaling. In each figure, X-axis represents the number of days after the start of the simulation, and Y-axis the ratio of total CO_2 mass variation to its starting value.
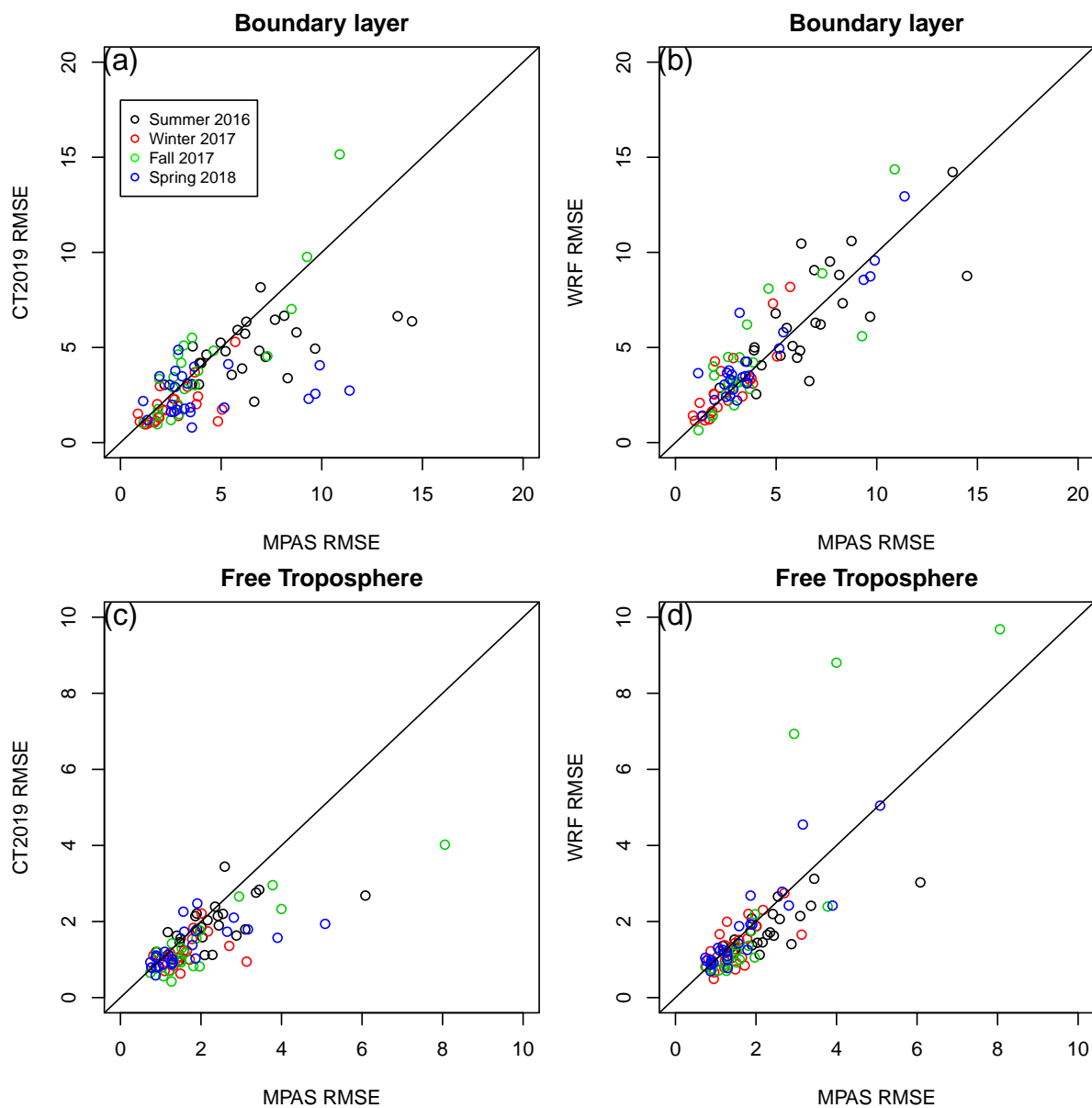
Figure 4. Comparison of model simulated CO_2 RMSE from MPAS with that from WRF-Chem and CT2019. The two figures on the top panel are the results from the boundary layer comparison and figures from the bottom panel are from the free troposphere. The RMSE comparison between MPAS and CT2019 are on the left side (a, c), and comparison between MPAS and WRF-Chem are on the right side (b, d). In each figure, a open circle represents model validation from one day's aircraft measurement and the color of the circle indicates the ACT campaign season it belongs to. All four subplots use the same legend as in the Fig. 4a
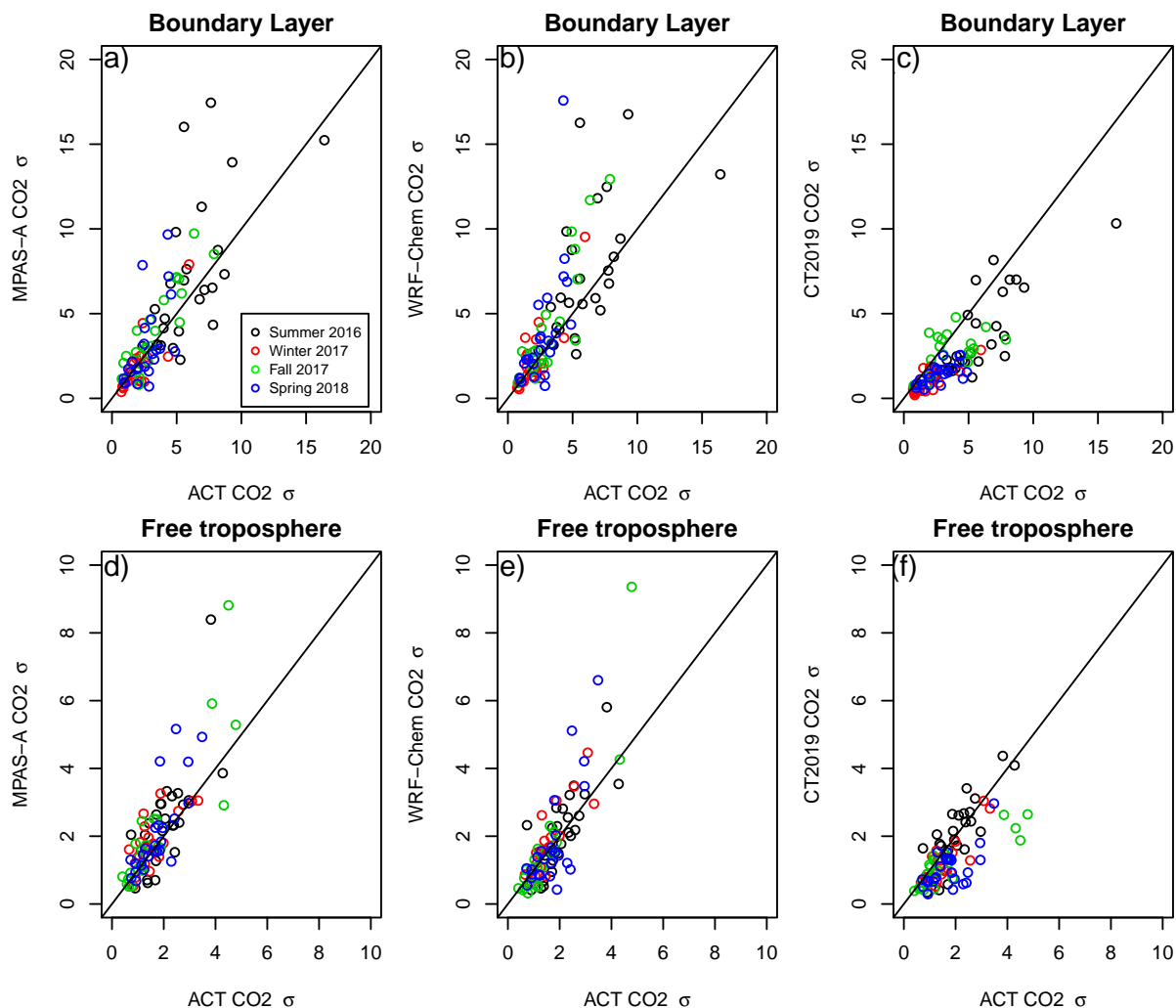
Figure 5. Comparison of standard deviation (σ, unit ppm) of aircraft observed CO_2 against that simulated by MPAS (a,d), WRF (b,e), and CT2019 (c,f). The comparison of standard deviation in boundary layer are in the top panels (a,b,c) and comparison in the free troposphere are in the bottom panel (d,e,f). In each subplot, a open circle represents one day's result and the color of the circle indicates its campaign season. All six subplots share the the legend in Fig. 11a.
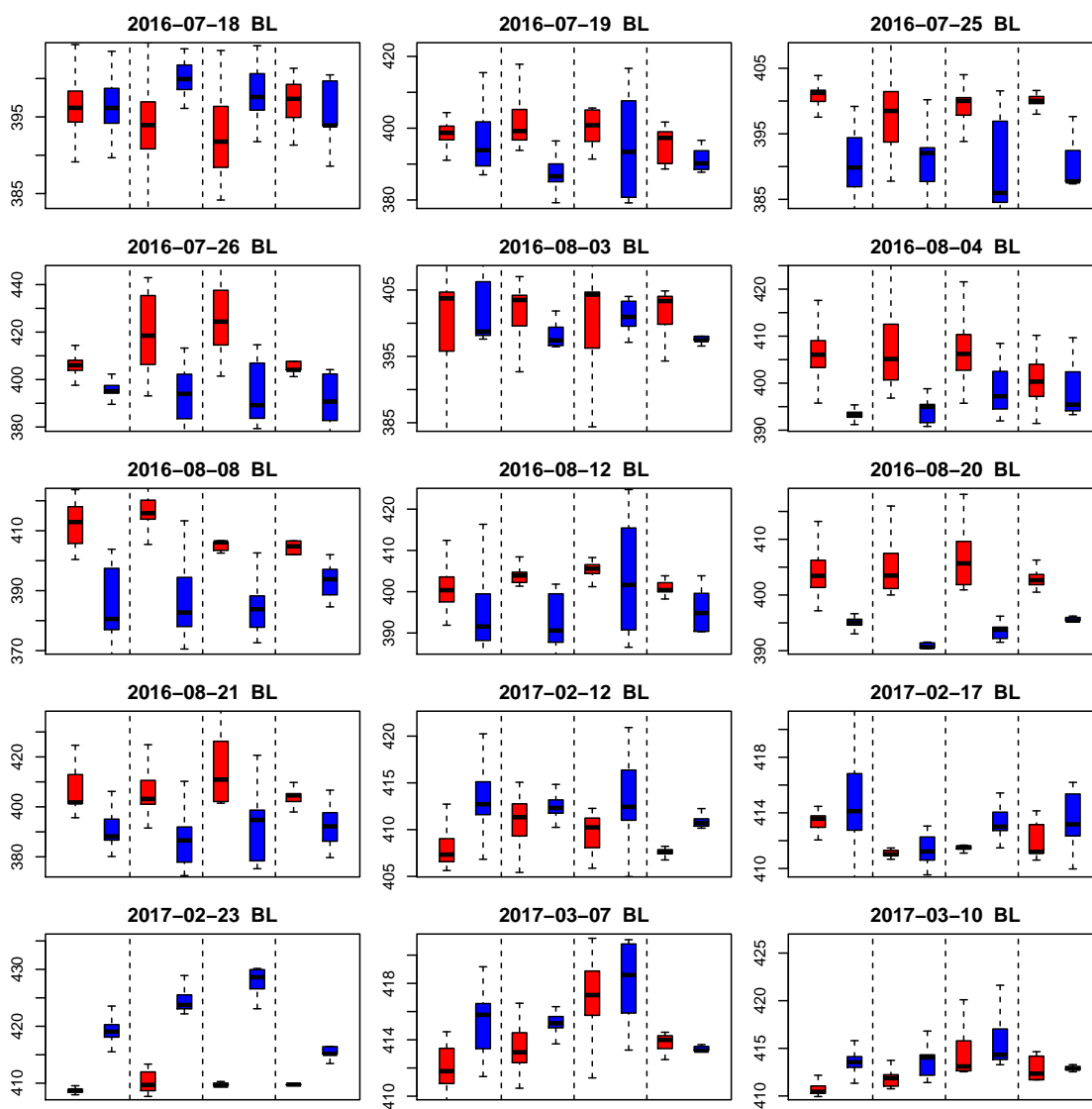
Figure 6. Box plots comparing mean boundary layer (BL) CO_2 mole fraction of the warm sector (red color) and cold sector (blue color) for 15 frontal crossing flights from summer 2016 and winter 2017 ACT campaign seasons. The flight date of each plot is labeled in its title. Data are combined when both aircraft (C130 and B200) took measurement for a given day. Each sub-figure is separated into four groups by the dotted lines: the first group is from ACT observations, the second is MPAS simulation, the third is WRF-Chem simulation, and the last is CT2019. In each boxplot, the bottom and top edge of the box represent the 1st (Q1) and 3rd (Q3) percentiles, the horizontal line represent the median, the ends of the whisker represents Q1-1.5×IQR and Q3+1.5×IQR respectively, where IQR=Q3-Q1.
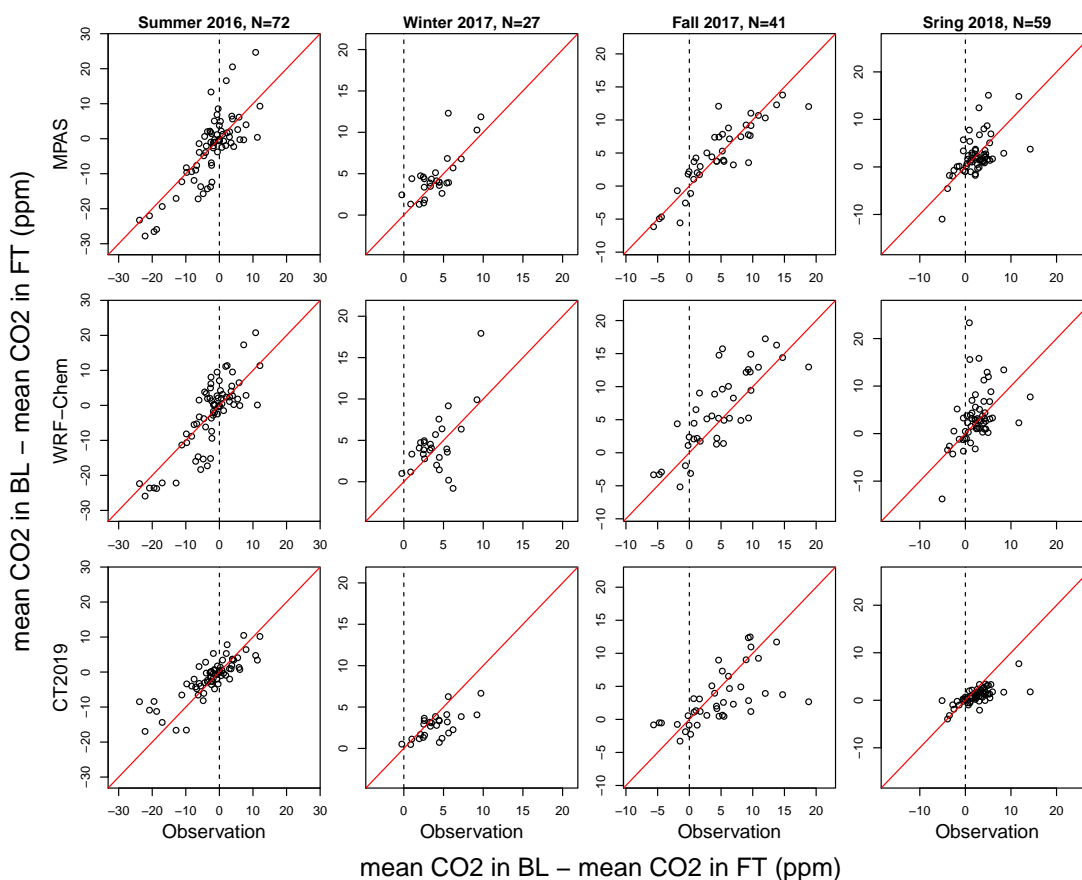
Figure 7. The difference of mean CO_2 mole fraction between boundary layer (BL) and free troposphere (FT) ($\Delta[CO_2] = [CO_2]_{BL} - [CO_2]_{FT}$) at vertical profiling flight legs. In each subplot, each open circle represents an individual vertical profiling flight leg, and its values on the X-axis and Y-axis represent its $\Delta[CO_2]$ value from the aircraft observations and the model simulation respectively. $\Delta[CO_2]$ from MPAS simulations are the first row, WRF-Chem the second row, and CT2019 the third. The four columns in the figure are for the four ACT campaign seasons. The number of vertical profiles in each season is labeled in the column title. The vertical dashed line marks where $\Delta[CO_2] = 0$ based on the aircraft measurements.
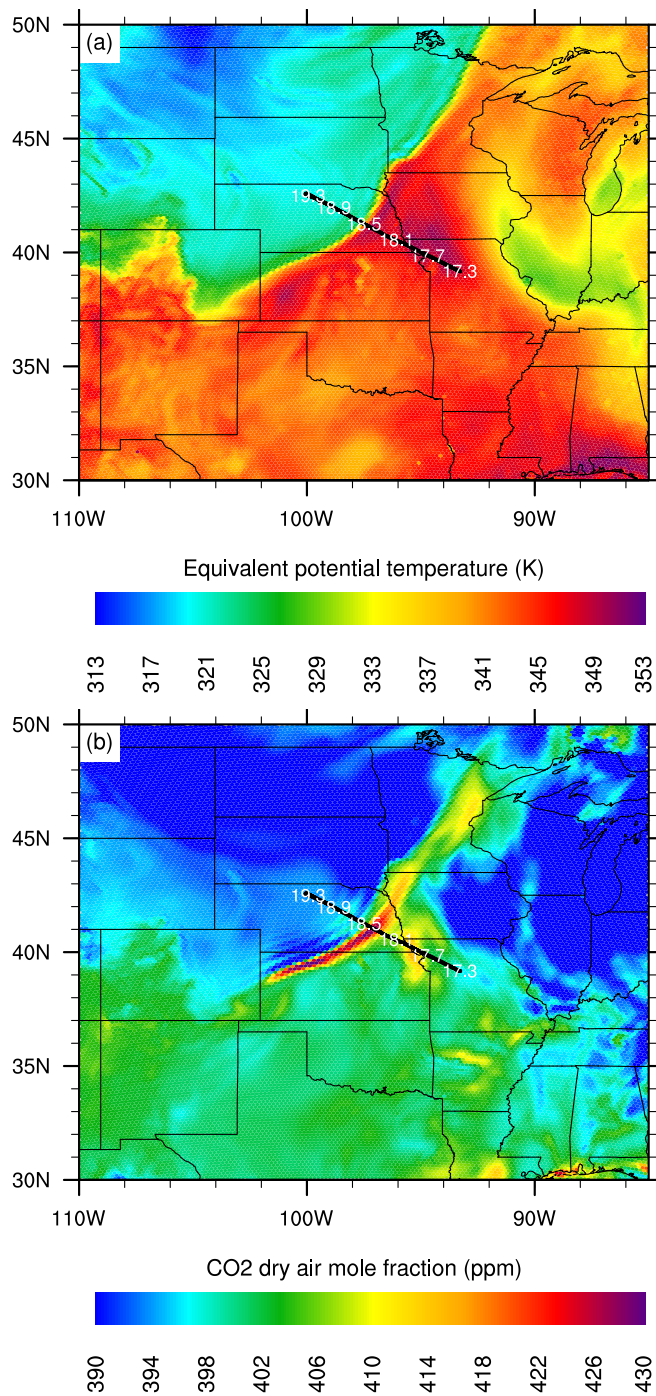
Figure 8. MPAS simulated equivalent potential temperature (θ_e, top panel) and CO_2 mole fraction (bottom panel) at 18:00 UTC 4 August 2016. Both figures are plotted at MPAS 6th vertical level, which is about 400 meters above the ground.
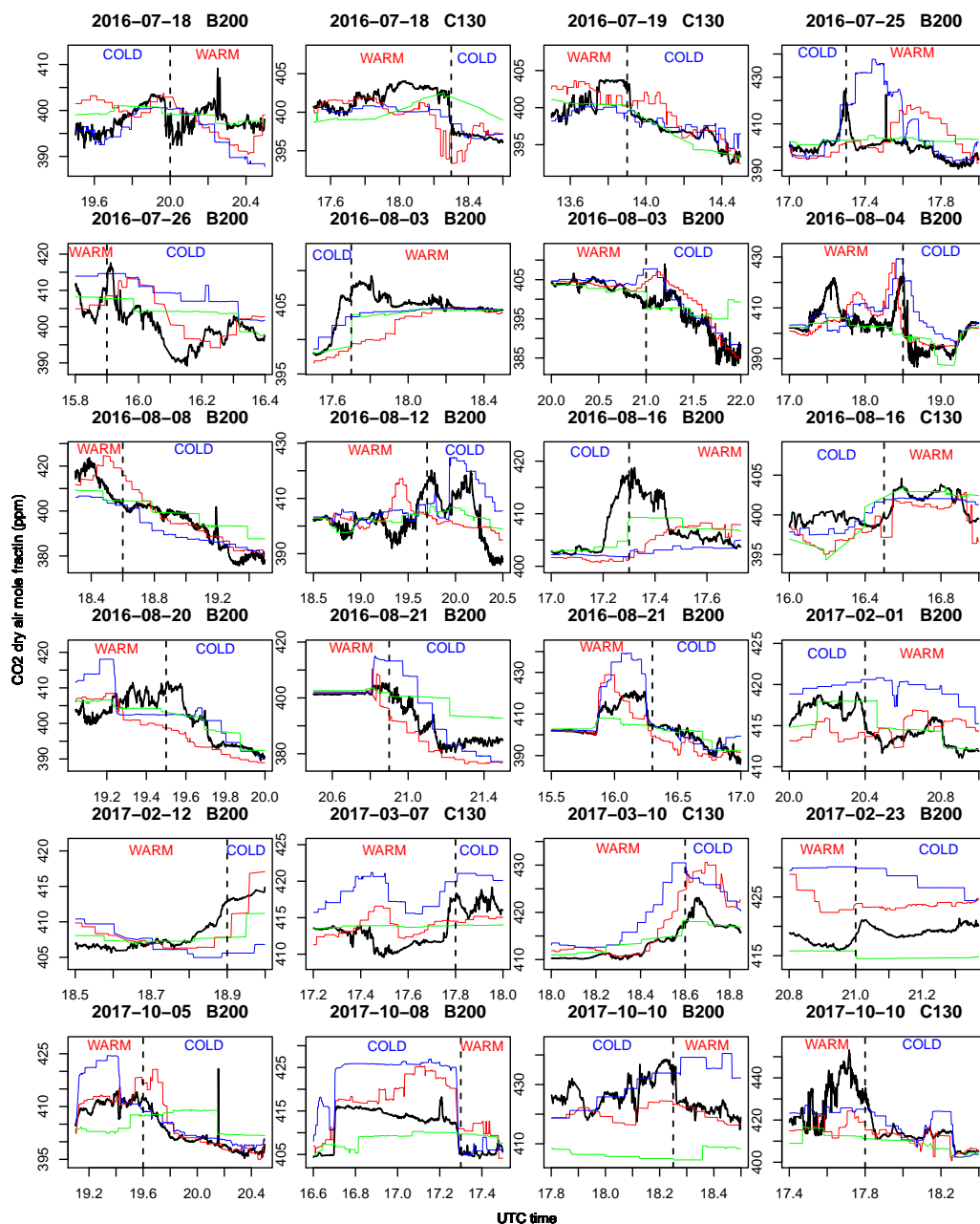
Figure 9. Comparison of CO_2 mole fraction in frontal-crossing level-leg flights in boundary layer between ACT aircraft measurements and model simulations. Flight date and aircraft type are labeled in title for each flight leg. In each figure, X-axis is UTC time, and Y-axis is CO_2 mole fraction (ppm). Aircraft measurements are in black, MPAS in red, WRF-Chem in blue, and CT2019 in green. The vertical dotted line in each figure marks the approximate location of boundary between warm and cold sectors, which are labeled as 'WARM', and 'COLD' respectively.
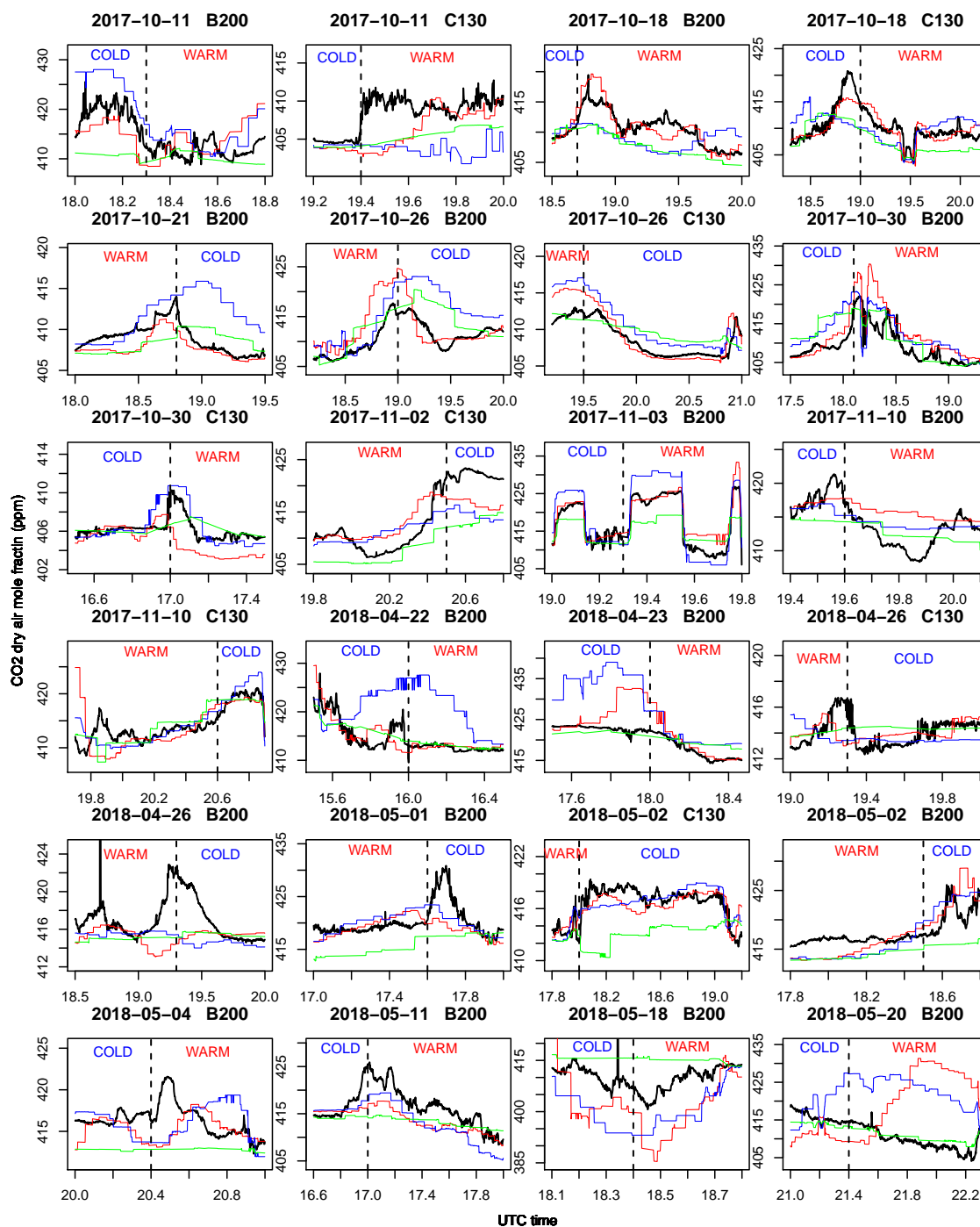
Figure 9. Continued from Fig. 9
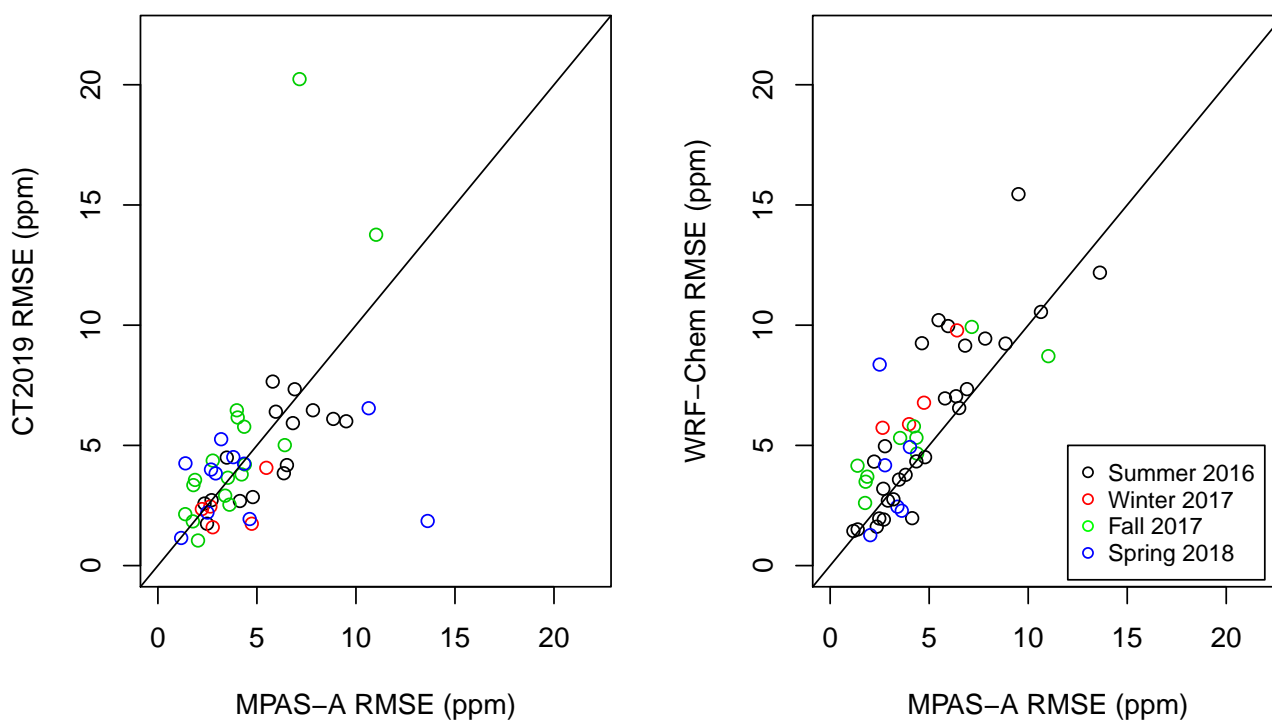
Figure 10. Comparison of RMSEs of model simulated CO2 at front-crossing horizontal flight legs (Figs. 9 and 9). Each open circle represent a horizontal flight leg, and its color represent the ACT campaign seasons. Comparison of RMSE between MPAS and CT2019 is in the left figure, and comparison between MPAS and WRF-Chem the right figure.
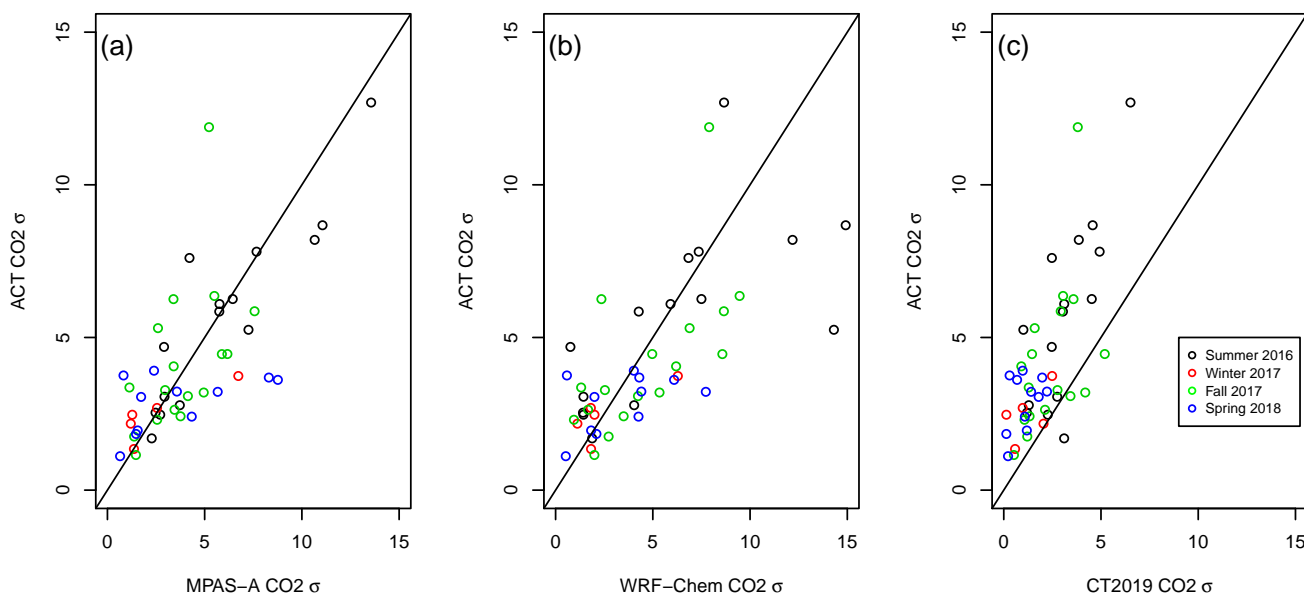
Figure 11. Comparisons of CO_2 mole fraction standard deviation (σ, unit in ppm) between aircraft measurement and model simulations: MPAS (a), WRF-Chem (b), and CT2019 (c). In each figure, the X-axis is σ of CO_2 mixing ratio from aircraft measurements, the Y-axis from a model. Each circle represent front-crossing horizontal flight leg in Figs. 9 and 9 and its color represent the ACT campaign season.

January 2014
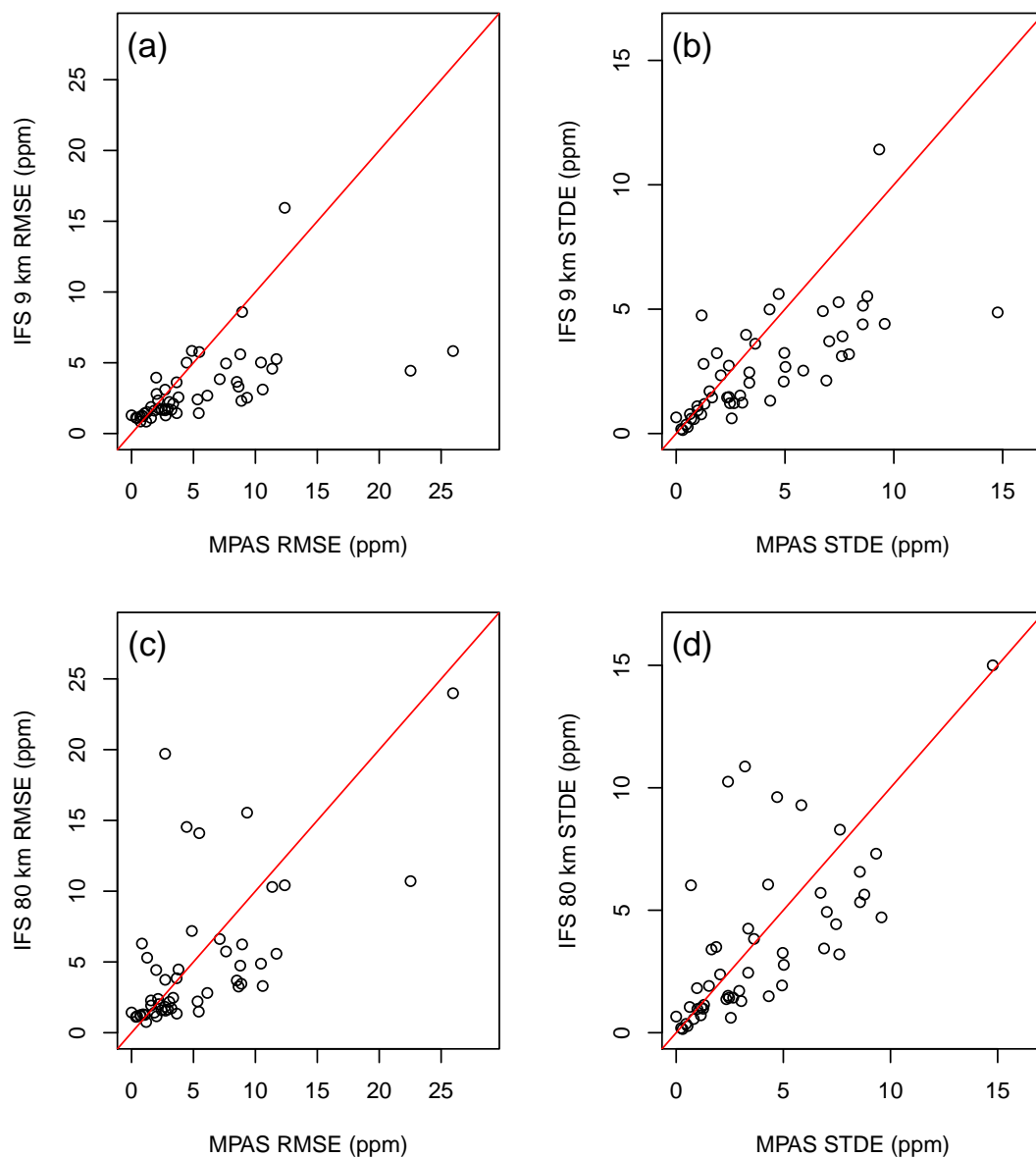
Figure 12. Comparison of model simulated hourly CO_2 accuracy (RMSE and STDE) between MPAS and IFS at 50 surface and tower stations. Each open circle in the figures represent a station. Comparison of MPAS with the IFS 9 km resolution simulations are in the top panel (a and b), and comparison with IFS 80 km resolutions simulations are in the top panel (c and d).
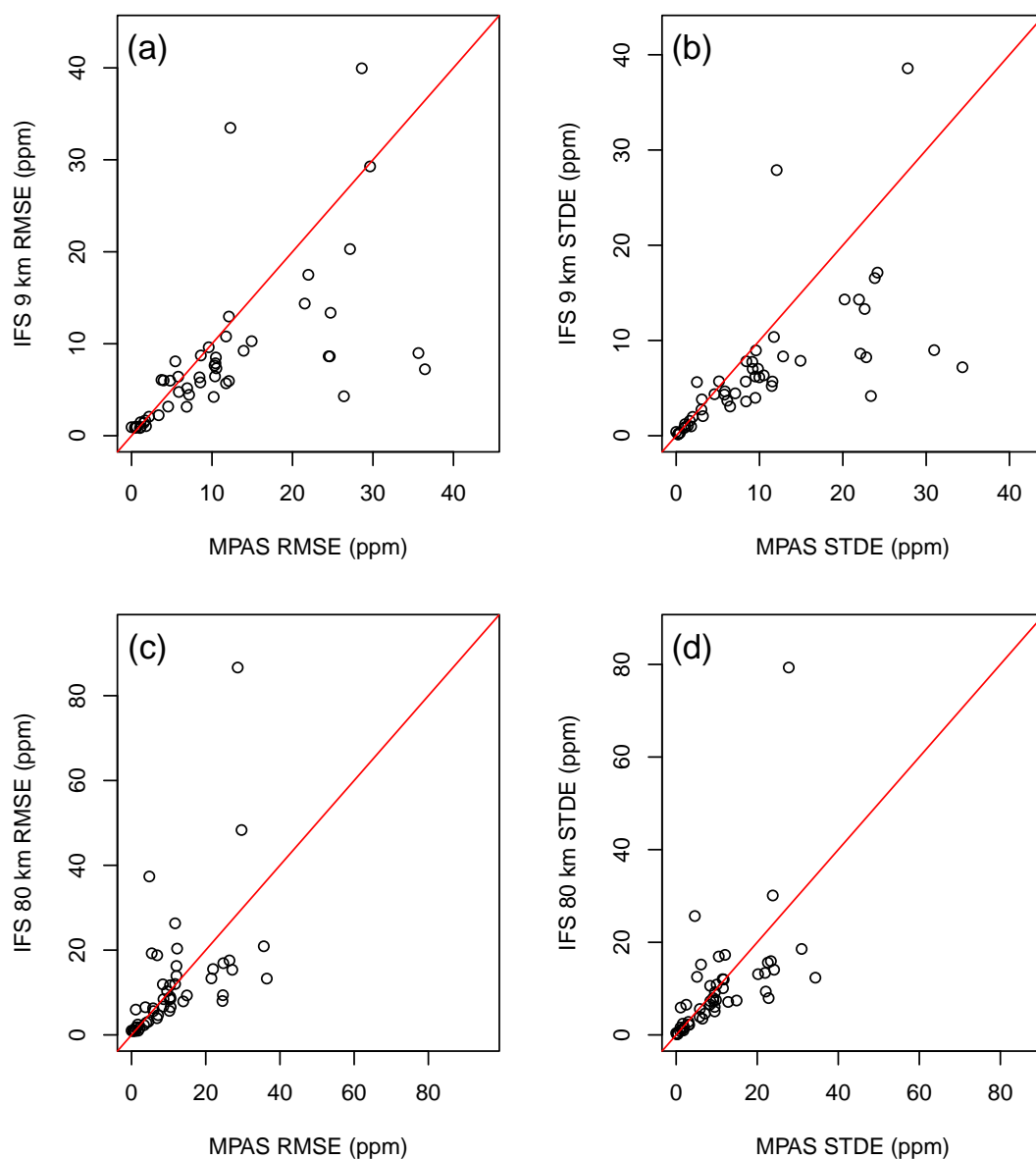
Figure 13. Same as Fig. 12, but for the month of July 2014

Table 1. MPAS CO_2 transport model simulation physical parameterizations summary.

Parameterization	Option Used	References
Longwave	RRTMG LW	Iacono et al. (2008)
Shortwave	RRTMG SW	Iacono et al. (2008)
PBL	YSU	Hong et al. (2006)
Surface layer	Monin-Obukhov	
Land Surface Model	Noah	Chen and Dudhia (2001)
Cumulus	Kain-Fritsch	Kain (2004)
Microphysics	WRF Single Moment 6-class	Hong and Lim (2006)

Table 2. The duration of four ACT aircraft campaign seasons and their corresponding MPAS simulations

	MPAS CO_2 simulation		ACT campaign season	
	Start	End	Start	End
Summer 2016	Jul 15	Aug 31	Jul 18	Aug 28
Winter 2017	Jan 29	Mar 12	Feb 01	Mar 10
Fall 2017	Oct 01	Nov 15	Oct 03	Nov 13
Spring 2018	Apr 10	May 23	Apr 12	May 20

Table 3. Evaluation of MPAS simulated horizontal wind using NOAA IGRA radiosonde data. Radiosonde data from 457 stations over the globe are used for the evaluation. Wind speed and direction are compared at 00:00 UTC and 12:00 UTC at four pressure levels (1000, 850, 500, and 200 hPa) for each day of the MPAS simulation. The number of data samples (N) are smaller at 1000 hPa because some stations are located above that pressure level.

	Pressure level	Mean RMSE vector wind (m/s)	RMSE Wind speed(m/s)	Bias Wind speed(m/s)	Mean difference Wind direction °	N
January 2014	1000 hPa	3.83	2.92	0.89	31.00	8,856
	850 hPa	4.04	2.96	-0.45	23.08	22,369
	500 hPa	3.72	2.66	-0.50	12.98	23,222
	200 hPa	4.38	3.07	-0.58	8.36	22,795
July 2014	1000 hPa	3.47	2.50	0.27	32.94	7504.00
	850 hPa	3.56	2.55	-0.51	27.12	22832.00
	500 hPa	3.39	2.39	-0.59	17.89	23745.00
	200 hPa	4.19	2.99	-0.55	12.19	23455.00

Table 4. Comparison of mean and standard deviation (in parenthesis) of CO_2 mole fraction (ppm) in the boundary layer between the warm and the cold sectors. The statistics for ACT aircraft measurements are in the first column, MPAS the second column, WRF-Chem the third column, and CT2019 the last column.

	ACT		MPAS		WRF-Chem		CT2019	
	warm	cold	warm	cold	warm	cold	warm	cold
2016-07-18	396.8(3.5)	396.6(3.2)	393.3(5.0)	400.1(1.8)	392.2(5.1)	398.4(3.3)	397.1(2.6)	395.6(3.2)
2016-07-19	398.3(3.1)	396.6(8.0)	401.6(6.9)	390.4(11.4)	400.1(4.2)	394.3(13.5)	395.9(5.0)	391.1(3.3)
2016-07-25	400.8(2.3)	390.4(4.2)	397.3(5.4)	391.3(4.6)	399.2(2.7)	389.9(6.3)	400.0(1.4)	390.8(4.3)
2016-07-26	405.9(4.5)	396.1(3.1)	420.6(15.2)	392.9(10.3)	424.7(14.2)	393.9(11.3)	405.2(2.1)	391.8(8.5)
2016-08-03	399.8(7.0)	401.8(4.2)	400.4(6.2)	398.0(1.5)	400.8(6.3)	401.1(2.0)	401.8(3.3)	398.2(1.8)
2016-08-04	407.3(5.7)	393.5(2.2)	407.0(7.6)	394.2(2.2)	407.5(7.3)	399.8(7.6)	401.1(4.1)	397.8(5.3)
2016-08-08	412.2(6.4)	385.3(10.9)	416.7(5.0)	386.8(10.5)	405.1(1.6)	383.9(7.4)	404.1(1.9)	392.6(5.2)
2016-08-12	401.4(5.5)	395.1(9.5)	404.9(4.0)	393.1(5.5)	405.4(1.7)	402.8(12.8)	401.0(1.2)	394.8(4.6)
2016-08-20	404.0(4.0)	395.1(1.1)	404.6(3.9)	390.9(0.4)	406.6(4.9)	393.3(1.3)	402.8(1.5)	396.0(1.0)
2016-08-21	406.5(7.2)	390.7(7.3)	408.1(13.8)	386.3(9.1)	414.8(14.0)	392.4(13.8)	404.2(3.8)	392.5(7.4)
2017-02-12	408.1(2.1)	414.2(4.2)	411.0(2.3)	412.6(2.4)	409.7(1.9)	413.1(4.2)	407.6(0.7)	410.4(1.4)
2017-02-17	413.5(0.8)	414.8(2.7)	411.1(0.2)	411.4(1.0)	411.5(0.2)	413.2(1.1)	411.9(1.0)	413.7(1.8)
2017-02-23	409.4(1.6)	419.1(1.6)	410.3(1.7)	424.7(4.6)	409.8(0.4)	428.2(2.0)	409.8(0.1)	415.6(0.8)
2017-03-07	412.0(1.3)	415.2(1.9)	413.5(1.6)	415.3(0.7)	417.4(2.2)	418.4(2.3)	413.8(0.7)	413.4(0.2)
2017-03-10	410.8(0.8)	413.6(1.0)	411.7(0.7)	414.1(2.5)	414.2(2.2)	416.2(4.2)	413.0(1.2)	413.1(0.7)

Table 5. Comparison of observed and modeled difference of the mean CO2 between boundary layer (BL) and free troposphere (FT) ($\Delta[CO_2] = [CO_2]_{BL} - [CO_2]_{FT}$). The RMSE and standard deviation are calculated by the comparisons between observation and models for each model and each season (Fig. 7)

	Num of profiles	RMSE (ppm)			Standard deviation (ppm)			
		MPAS	WRF-Chem	CT2019	observation	MPAS	WRF-Chem	CT2019
Summer 2016	72	5.96	5.75	4.18	7.33	10.13	10.15	5.52
Winter 2017	27	1.96	2.93	2.13	2.34	2.84	3.65	1.56
Fall 2017	41	2.54	3.99	4.47	5.40	5.11	6.14	4.16
Spring 2018	59	5.11	5.81	2.82	3.28	5.57	6.14	1.76

Table 6. Evaluation of MPAS simulated horizontal wind using radiosonde observations at 457 stations located across the globe. Wind speed and direction are compared at 00:00 UTC and 12:00 UTC at four pressure levels (1000 850, 500, and 200 hPa) for each day of the MPAS simulation. Note the number of data samples (N) is smaller at 1000 hPa because some stations are located above that pressure level.

	Pressure level	Mean RMSE vector wind (m/s)	RMSE Wind speed(m/s)	Bias Wind speed(m/s)	Mean difference Wind direction °	N
Summer2016	1000 hPa	3.87	2.80	0.63	34.15	11,630
	850 hPa	3.75	2.62	-0.41	28.70	34,107
	500 hPa	3.58	2.51	-0.57	18.84	35,213
	200 hPa	4.58	3.27	-0.52	13.40	34,732
Winter2016	1000 hPa	4.02	2.93	1.01	32.00	11,415
	850 hPa	4.11	2.92	-0.32	25.28	27,957
	500 hPa	4.03	2.82	-0.43	14.67	28,977
	200 hPa	4.55	3.23	-0.48	9.79	28,401
Fall2017	1000 hPa	3.76	2.78	0.99	32.00	12,396
	850 hPa	4.05	2.89	-0.38	25.38	31,964
	500 hPa	3.92	2.74	-0.45	14.93	32,881
	200 hPa	4.63	3.22	-0.46	10.39	32,252
Spring2018	1000 hPa	3.98	2.93	0.89	33.80	10,763
	850 hPa	4.05	2.84	-0.30	27.85	29,886
	500 hPa	4.12	2.90	-0.42	17.24	30,914
	200 hPa	4.79	3.45	-0.46	12.96	30,257

Table 7. Continuous in-situ stations used for evaluating MPAS CO_2 simulation accuracy. NA denotes references that are not available.

Station ID	Latitude	longitude	altitude (m a.m.s.l)	intake (m a.g.l)	Reference
alt	82.45 N	62.51 W	200	10	Worthy et al. (2003)
brw	71.32 N	156.61 W	11	16	Peterson et al. (1986)
cby	69.13 N	105.06 W	35	12	NA
inu	68.32 N	133.53 W	113	10	Worthy et al. (2003)
pal	67.97 N	24.12 E	560	5	Hatakka et al. (2003)
bck	62.80 N	116.05 W	179	60	NA
chl	58.74 N	94.07 W	29	60	Worthy et al. (2003)
llb	54.95 N	112.45 W	540	10	Worthy et al. (2003)
etl	54.35 N	104.99 W	492	105	Worthy et al. (2003)
mhd	53.33 N	9.90 W	5	24	Ramonet et al. (2010)
wao	52.95 N	1.12 E	20	10	Wilson (2013)
ces	51.97 N	4.93 E	-1	207	Vermeulen et al. (2011)
est	51.66 N	110.21 W	707	3	Worthy et al. (2003)
fsd	49.88 N	81.57 W	210	40	Worthy et al. (2003)
cps	49.82 N	74.98 W	381	8	Worthy et al. (2003)
esp	49.38 N	126.54 W	7	40	Worthy et al. (2003)
kas	49.23 N	19.98 E	1989	5	Necki et al. (2003), Rozanski et al. (2014)
ssl	47.92 N	7.92 E	1205	12	Schmidt et al. (2003)
hun	46.95 N	16.65 E	248	115	Haszpra et al. (2001)
jfj	46.55 N	7.99 E	3570	10	Schibig et al. (2015)
lef	45.95 N	90.27 W	472	396	Andrews et al. (2014)
puy	45.77 N	2.97 E	1465	10	Lopez et al. (2015)
amt	45.03 N	68.68 W	53	107	Andrews et al. (2014)
egb	44.23 N	79.78 W	251	3	Worthy et al. (2003)
wsa	43.93 N	60.01 W	5	25	Worthy et al. (2003)
vac	42.88 N	3.21 W	1086	20	Morgui et al. (2013)
tpd	42.64 N	80.56 W	231	35	Worthy et al. (2003)
dec	40.74 N	0.79 E	1	10	Morgui et al. (2013)
hdp	40.56 N	111.65 W	3351	17.7	Stephens et al. (2011)
spl	40.45 N	106.73 W	3210	9.1	Stephens et al. (2011)
gic	40.35 N	5.18 W	1436	20	Morgui et al. (2013)
nwr	40.05 N	105.59 W	3523	3.5	Stephens et al. (2011)
bao	40.05 N	105.00 W	1584	300	Andrews et al. (2014)
ryo	39.03 N	141.82 E	260	20	Tsutsumi et al. (2005)
snp	38.62 N	78.35 W	1008	17	Andrews et al. (2014)
wgc	38.26 N	121.49 W	0	483	Andrews et al. (2014)
sgc	36.70 N	5.38 W	850	20	Morgui et al. (2013)
sct	33.41 N	81.83 W	115	305	Andrews et al. (2014)

Table 7. Continuation of Table 7.

Station ID	Latitude	longitude	altitude (m a.m.s.l)	intake (m a.g.l)	Reference
wkt	31.31 N	97.33 W	251	457	Andrews et al. (2014)
izo	28.31 N	16.50 W	2373	13	Gomez-Pelaez and Ramos (2005)
yon	24.47 N	123.01 E	30	20	Tsutsumi et al. (2005)
mnm	24.29 N	153.98 E	8	20	Tsutsumi et al. (2005)
mlo	19.54 N	155.58 W	3397	40	Thoning et al. (1989)
smo	14.25 S	170.56 W	42	10	Halter et al. (1988)
cpt	34.35 S	18.49 E	230	30	Brunke et al. (2004)
ams	37.80 S	77.54 E	55	20	Gaudry et al. (1991)
cgo	40.68 S	144.69 E	94	70	Francey et al. (2003)
cya	66.28 S	110.52 E	47	7	Loh et al. (2017)
syo	69.00 S	39.58 E	14	8	NA
spo	89.98 S	24.80 W	2810	10	Conway and Thoning (1990)